

Using Protostellar Outflow Chemistry to Probe Extraterrestrial Ice Abundances

A study in the chemical morphology of L1551 IRS5

A Thesis Presented

by

Jamie A. Weisenberg

to

The Department of Astrophysics &

The Department of Earth and Planetary Sciences

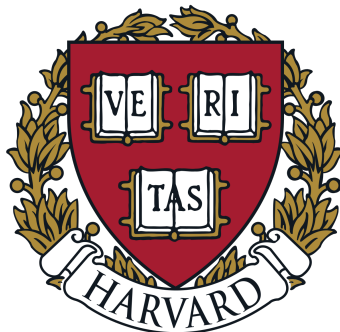
in partial fulfillment of the requirements

for a degree with honors

of Bachelor of Arts

April 2020

Harvard University



1. ABSTRACT

Understanding the chemistry that occurs during solar system formation can give insight to how life on earth developed. Most of this chemistry develops on the icy mantles of interstellar grains. To study it we can either observe the species directly in other star systems (in the gas or ice phase) or use models to simulate the process. To detect molecules in space, we can observe emission spectra when a molecule emits a photon or absorption spectra as a molecule absorbs a photon. While the most complex chemistry in space occurs on icy dust grains, it is difficult to detect molecules in the ice phase due to observational limitations. Specifically, the absorption features of ice chemistry are harder to detect than gas phase spectra. While we see complex molecules in the icy interstellar medium and comets, the most complex molecule we can confidently identify in the ice phase using vibrational spectroscopy is methanol (CH₃OH). Thus to observe more complex molecules than methanol, we look to find alternative methods of constraining interstellar ice abundances. We present one such alternative approach, using protostellar outflows as a proxy for ice chemistry. These outflows can sputter and sublimate ice into the gas phase without inducing thermal chemical changes. We can thus observe this gas as a measurement of the material that has left the solid phase.

Recent studies suggest that L1551 IRS5 shows evidence of chemically rich outflows. Here we use an interferometric survey at radio wavelengths that spans 50 GHz of bandwidth from around 290-365

GHz to examine the chemical morphology of the outflow regions. Specifically, we analyze the spectra of L1551 IRS5 to determine molecular abundances throughout the outflow of the protostar, and image the emission locations to compare the chemistry and morphology of different molecules in the region. We then compare abundances of different regions to other protostellar systems and comets. We compare these outflows to the chemical complexity in comets to test the validity of using shocks to probe the ice cloud of L1551 IRS5. We find a rich chemical profile of many species in the outflow of L1551 IRS5 consistent with previous structural studies of the region. Our analysis shows significant variation in chemical richness and column densities along the outflow as a function of radial distance from the center protostar. Additionally, six of the nine most abundant species present in the outflow are also present in comet 67P/C-G. We conclude that this similarity may suggest that by probing the outflow in L1551 IRS5, we are indeed able to proxy the ice chemistry of the surrounding molecular cloud to better understand the overall chemistry of stellar evolution.

1. Abstract	2
2. Introduction	6
2.1. Stellar Evolution	7
2.1.1. Solar-Type Star Formation	7
2.1.2. Chemistry During Star Formation	8
2.1.3. Chemistry in Protostellar Outflows	10
2.2. An interesting Protostar: L1551 IRS5	12
2.3. The Importance of Comets	14
2.4. Goals	18
3. Methods	19
3.1. Millimeter Interferometry	19
3.2. L1551 Observation	21
3.2.1. Imaging	21
3.2.2. Making Spectra	25
3.2.3. Analyzing Spectra	27
4. Results	29
4.1. Structure of Outflow	29
4.2. Line Identification	34
4.3. Molecular Emission Across outflow	37

	5
4.3.1. Distribution of Carbon Monoxide	37
4.3.2. Integrated Line Emission for Prominent Species	40
4.4. Extracting Abundances and Temperature with Rotational Diagrams	43
4.4.1. Rotational Diagrams across outflows	45
5. Discussion	50
5.1. Spatially Resolved Chemistry Along Outflows	50
5.2. Species Comparison with Comets	53
6. Conclusions	60
7. Acknowledgements	63
8. Appendix	64

2. INTRODUCTION

Many open questions remain in our understanding of the chemistry related to the origin of life. To help address this, we seek to understand how unique the chemical composition of our solar system is relative to other star systems. Much of the record of the chemical evolution of the solar system has been lost to time through chemical reprocessing. However, since comets are made out of the primordial material of the solar system, they can probe the previous stages of our origin as the building blocks for early planetary bodies (Lissauer 1993). In this introduction, we seek to understand how comets are produced through stellar evolution. It is important to consider how the ice chemistry evolves over stellar evolution, and discuss the ice in cold molecular clouds and how it is from this material that stars form. Specifically, we investigate why ice chemistry (solid-phase chemistry) in particular is crucial to forming complex molecules. With context on ice chemistry we make our way through the story of star formation. Within star formation, we focus on the protostar phase to investigate this ice chemistry. We discuss the unique characteristics of protostars and why they make a good target for this study. Specifically, we focus on the outflows and shocks seen in protostars and the affects these can have on chemical compositions. Next, we move on to discuss our observation target, L1551 IRS5, providing background and previous work on this source and motivate why it is specifically a good protostar to observe. We then look to comets as a point of comparison for observable ice chemistry and test for similarity to our protostar. To understand this comparison, we discuss comets in terms of their significance as a link between earlier stages of solar system formation and the present. We outline how comets form, how we know their chemistry, and what species have been observed on comets. Finally, we outline our goals for the project and discuss an outline for the subsequent sections of this thesis.

2.1. *Stellar Evolution*

2.1.1. *Solar-Type Star Formation*

A sun-like star begins its formation process from interstellar medium in a dense cloud. The majority of baryonic matter in the universe is found in galaxies, composed of stars and interstellar medium. This material between stars, which makes up about 10% of matter, hosts complex molecules and rich chemistry (Herbst & Millar 2008). The Interstellar Medium can exist in cold, warmer, and hot regions. In warm regions (50-100 K), exist diffuse clouds. Diffuse clouds are transparent and are generally homogeneous, but can contain colder cores. Denser clouds are cold (5-50 K) and are opaque at ultraviolet and visible wavelengths. These cold conditions allow for chemical interactions between gas and ice forming on the dust grains. The cold temperatures may be prohibitive to chemical efficiency as there is less energy to get over reaction activation barriers. However, the increase in density still makes ice chemistry more efficient than gas-phase chemistry as collisions are more frequent.

Over time, this material coalesces, forming a cold, dense core. Over time, this dense core collapses under gravity, to form a protostar. This collapse occurs when the material reaches the Jeans criteria in length and mass when a cloud's gravitational energy exceeds twice the kinetic energy as following the Virial theorem (Shu et al. 1987):

$$2K + U = 0 \tag{1}$$

This assumes the absence of rotation, external gas pressure, turbulence or magnetic fields. As the material reaches these Jeans limits, it undergoes a collapse where all elements of the cloud take the same freefall time to collapse. At this point, the center of the protostar is cooler than the critical temperature to begin nuclear fusion of hydrogen. Over the span of stellar evolution, the core heats

up to continue on to become a main sequence star. A protostar removes angular momentum from the infalling gas, enabling gas to accrete in a disk and to build up the star. Accreting material will form a disk surrounding the star and can eventually form planetary systems, such as ours (Shu et al. 1987).

Once formed, protostars can host unique physical properties. One such feature is a set of bipolar jets. As the gas and dust of a dense cloud accrete to form a protostar, it drives out material in bipolar jets due to conservation of angular momentum and launching along the magnetic field lines. Bipolar jets and their associated magnetic fields carve out three dimensional cavities free of the material in the surrounding cold molecular cloud. Magnetic forces, originating from the protostar, can then eject material from the core by accelerating gases to high velocities, thus creating outflows, the material flowing outward from the central protostar (Arce et al. 2007).

2.1.2. *Chemistry During Star Formation*

To investigate the chemistry during this process more closely, we turn to the earliest stage of the dark dense interstellar clouds. Ice chemistry and gas chemistry lead to different molecule formation and chemical abundances. In space, species are at a low density, making gas phase chemical processes limited and slow. Traditionally terrestrial chemical reactions often require a third body to absorb the energy released of forming bonds. When only two bodies collide and form a bond, a significant amount of energy is released. Without a third body to absorb this energy, the bond between the species is likely to break apart. In the low-densities common in interstellar environments, a direct collision of all three bodies is rare. The build up of complex chemistry in the gas phase is slow and is dominated by ion-neutral chemistry. These limitations do not apply to Earth, as the high densities on earth allow for a higher probability of both 2 and 3-body collisions. In the interstellar

medium, atoms and molecules on ice and dust grains can also work around these limitations. The grain provides a surface and helpful divots to form and protect larger molecules and the ice shields the chemistry from disruptive UV-radiation.

Given the unique processes of ice chemistry, we seek to observe the ice in the interstellar medium. Using an infrared spectra, we can extract the average ice abundances from absorption features. In this regime of the electromagnetic spectrum, features can correspond to electronic, vibrational, or rotational transitions as a photon is emitted (emission spectroscopy) or absorbed (absorption spectroscopy). Absorption spectroscopy measures how much light is blocked from a background source. An example of this is measuring the dust in a molecular cloud in front of the light of a star. Figure 1 from [Boogert, et al. \(2015\)](#) shows an infrared spectra of massive YSO (young stellar object) AFGL 7009 S. This category of stellar object refers to protostars and pre-main sequence stars. YSO's around molecular clouds can be used as a background source for an emission spectra for the molecular cloud of interest. This spectra in Figure 1 uses the light emitted from YSO AFGL 7009 S to measure the absorption of the molecular cloud in front of the light source. Figure 1 depicts features of the most abundant species. While the species identified here are the straightforward cases, the figure does foreshadow the variety of modes which can cause a feature and the resulting complications in identifying more complex features.

Detecting ice abundances in space can be difficult as molecules in ice cannot rotate and therefore we must detect vibrational transitions in absorption. Larger molecules with confounding vibrations are particularly hard to detect as they experience heightened degenerate spectral features and significant blending. Larger molecules display overlapping lines, broad features, and unclear identifications ([Ruard et al. 2016](#)). Additionally, low abundances make them increasingly difficult to detect. Due

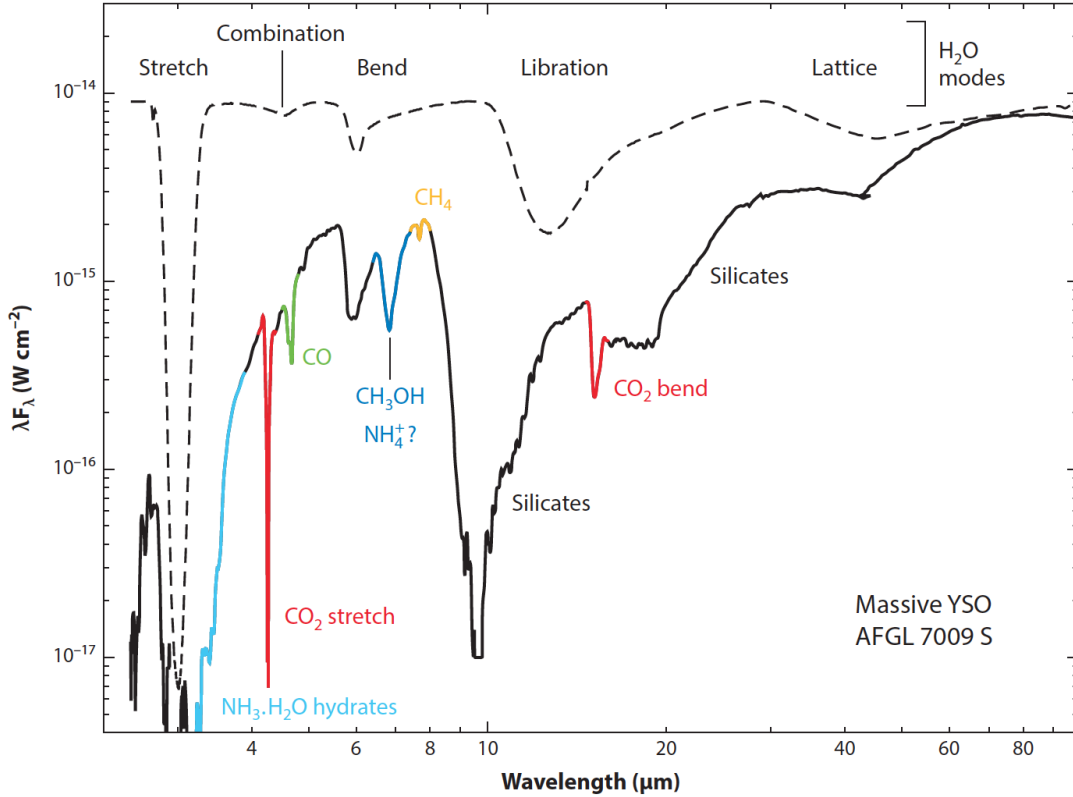


Figure 1: This figure from [Boogert, et al. \(2015\)](#) is an example infrared spectra showing the detection of different solid-phase vibrational absorption transitions of several molecules. Each dip in the curve corresponds to a decrease in flux from a background source as a species absorbs a photon at a known wavelength to these factors, only the abundances of six ice species have been well constrained. These species are H_2O , CO , CO_2 , CH_3OH , CH_4 , and NH_3 ([Öberg et al. 2011](#)). With the difficulty to constrain this chemistry, we look to molecules as they are desorbed into the gas phase through some physico-chemical process such as sputtering and sublimation [Burkhardt et al. \(2019\)](#).

2.1.3. Chemistry in Protostellar Outflows

Moving forward in star formation, protostars provide one such opportunity for ices to be put into the gas-phase. Outflowing material can collide with the enveloping cloud created by the cavities

formed by the jet. These collisions create thin compact areas of high temperature and density at the shock front (Suutarinen et al. 2014). These shock fronts can host complex processes including the sputtering of molecules off of the ices and high-temperature gas-phase chemistry. So, as we seek to understand ice chemistry, isolated outflows coming from protostars can be relatively simple laboratories for chemical comparisons. Additionally, investigating the radial dependence on gas-phase abundances can potentially be correlated to the temporal evolution within a shock.

Bow shocks are formed as a jet impacts the ambient material (Arce et al. 2007). Low-velocity shocks liberate molecules off of the ice and into the gas phase via sputtering without destroying most molecular bonds (Requena-Torres et al. 2006). Thus protostellar outflows with shocks can be a target for observing rich chemistry in particular. Studies have shown that protostellar shocks can enhance the gas-phase abundances of complex molecules such as NH_2CHO , CH_3CHO , CH_3OCH_3 , HCOOCH_3 , $\text{C}_2\text{H}_5\text{OH}$, and CH_3CN as these species are sputtered out of the ice into the gas. One such study by Burkhardt et al. (2016) examines the shocks of the low-mass protostar L1157, which has shown a bipolar outflow with ejections creating shocks in the surrounding dust cloud which contains the targeted ice. Burkhardt et al. (2019) divided the shock chemistry of L1157 into three classes: direct sputtering from grains (e.g., CH_3OH), shocks enhancing existing gas (e.g., HCO^+), and a combination of sputtering and gas-phase enhancement (e.g., HNCO).

2.2. An interesting Protostar: L1551 IRS5



Figure 2: L1551 cloud, with a blue circle around IRS5 as seen in [Fridlund \(2016\)](#), as Herbig-Haro objects. Deep $H\alpha$ and $[SII]$ images obtained by Bo Reipurth at the 8m Subaru telescope; color composite by Robert Gendler

One source that is particularly interesting is L1551 (Figure 2), a molecular cloud that has been observed for over 60 years. It is located 140 pc from Earth. In 1976, CO structure studies led to an interest in the IRS5 region of the L1551 cloud (circled in blue in Figure 2). Many follow-up studies with high resolution imagery then indicated that IRS5 contained a binary star system (e.g., [Bieging, & Cohen \(1985\)](#)), and was first imaged as a resolved continuum of the circumbinary ring and

circumstellar disks by [Cruz-Sáenz de Miera et al. \(2019\)](#). Since then, it has become an interesting target area for its proximity and signs of molecular complexity.

In 2009, [Wu et al. \(2009\)](#) did a comprehensive study of the physical structure of L1551 IRS5. They created a CO(2–1) image at $\sim 4''$ resolution which is equivalent to 600 AU, to study the structure of system. They used this image to interpret and model the system’s large outflow. They reported an X-shaped structure spanning $20''$ from center, an S-shaped structure spanning $10''$ from center with an opposite velocity pattern to the large-scale outflow, and a compact central region of $1.4''$. Figure 3 from [Wu et al. \(2009\)](#) depicts this 3D conical structure as derived from their study with CO. It shows the orientation of the system in the plane of observation along with the jets moving in opposite directions of the surrounding envelope material. The walls of the cones correspond with the limb brightening X, seen in 2D images as the telescope is looking through more material on the edges. [Wu et al. \(2009\)](#) discuss precession and reversed velocity direction of the jets, creating the S-shape structure of the system and perhaps indicating a potential 3rd component north or south of the system interacting gravitationally.

Other studies have looked at the chemistry of L1551 IRS5. In 1980, [Sandqvist, & Bernes \(1980\)](#) published a finding of formaldehyde in the region as a probe of the dust cloud. In their study, they found an increase in density toward the center of the region. Using H_2CO , they estimate a temperature on the periphery of 10 K, increasing to 23 K towards the center. [Fridlund et al. \(2002\)](#) continued to look at the chemistry of the central region using HCO^+ , H^{13}CO^+ , ^{12}CO and ^{13}CO . Using these features, they calculate the mass of the cloud (excluding the protostars) to be $2.5 M_{\odot}$. More recently, ALMA (Atacama Large Millimeter Array) observations have focused on the inner-most regions of the source.

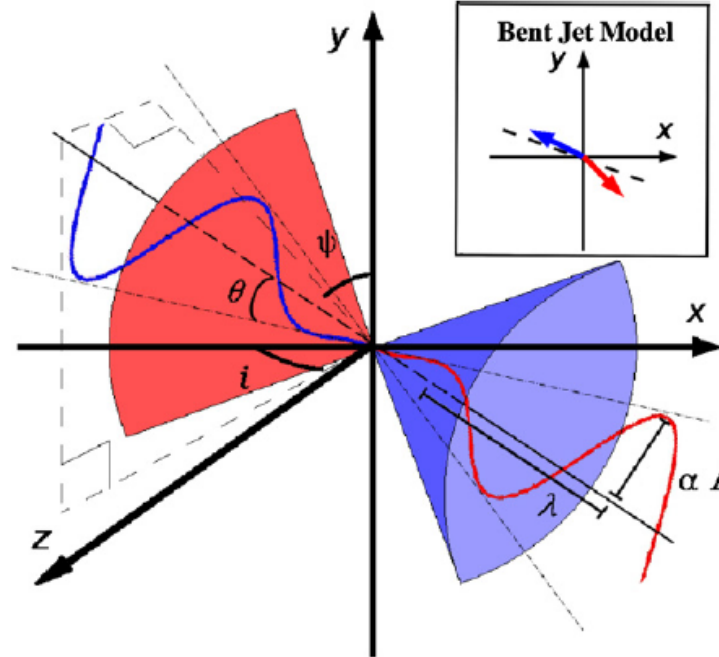


Figure 3: Structural representation of L1551 IRS5 conical outflows and precessing jets from Wu et al. (2009). The red and blue cones represent the doppler-shifted material flowing out from the center. The angles correspond to the orientation of the object in the plane of observation

2.3. The Importance of Comets

Tying it all together, we seek to assess the validity of using shocks in L1551 as a proxy of the surrounding ice material. One way we can do this is by making comparisons to comets as they are one of the best constrained direct observations of extraterrestrial ice chemistry. Comets are primarily composed of silicates and iron compounds or carbonaceous materials, forming from a conglomeration of tiny dust particles (Altwegg et al. 2019). Comets are known as “dirty snowballs” with nuclei of ice, rock, and large organics (Ehrenfreund, & Charnley 2000). As they are cold, they are great at housing rapidly producing ices. They are predominantly populated with H_2O , CO_2 , CH_3OH , and

CO ices (McGuire et al. 2016). The processing of these abundant ice species at the heightened pace of reactions is conducive to forming more complex organics.

Comets are believed to preserve their initial organic composition, thus reflecting the ice chemistry during planet formation. They retain ice chemistry from planetary formation with their surfaces and crevices and are able to maintain their ice in orbits further out from the star. If a comet then approaches closer to the star, it will be gradually warmed and sublimate the solid material into a gaseous coma surrounding the nucleus of the comet (Walsh et al. 2014). Studies suggest that comets are the link between ice chemistry and planet formation. Since we observe rich chemistry on comets, it has been proposed that cometary bombardment could be the source of Earth's initial necessary ingredients for life, bringing water to basic organics and amino acids (Mumma, & Charnley 2011). Studies in the deuterium-to-hydrogen ratio in comets show variation in comets in different areas of the solar system (Altwegg et al. 2019). This ratio can be used in comparison with the deuterium-to-hydrogen ratio of earth's oceans, furthermore securing that planets are not in isolation from the ice chemistry found on comets.

Recent missions of solar-system probes, orbiters, and landers have detected complex chemistry in comets including glycine, the simplest amino acid. Laboratory experiments suggest that amino acids can be formed in the ice mantles of dust grains at low temperatures (Garrod 2013). Amino acids are necessary for proteins, and consequently life here on earth. DNA is composed of four nucleotides, adenine, thymine, cytosine and guanine. DNA can then replicate itself and be transcribed to RNA. Codons of RNA translate to amino acids which make proteins.

In 2006, the Stardust spacecraft procured samples from the 81P/Wild 2 comet. These samples revealed an onslaught of organics including methylamine (NH_2CH_3), ethylamine ($\text{NH}_2\text{C}_2\text{H}_5$) and

glycine ($\text{NH}_2\text{CH}_2\text{COOH}$) (Elsila et al. 2009). In 2014, the Rosetta spacecraft entered an orbit of the comet 67P/Churyumov-Gerasimenko (67P/C-G). Remote mass spectrometry obtains key information on the composition of comet 67P/C-G. The Rosetta Mission revealed that 67P/C-G showed an abundance of volatiles, chemicals with low temperatures of evaporation (Rubin et al. 2019). Specifically, 67P/C-G was found to contain glycine, methylamine, and ethylamine (Altwegg et al. 2016). While a definitive origin of complex cometary volatiles is uncertain, evidence suggests they have stemmed from the ice chemistry in the interstellar medium (Bockelée-Morvan et al. 2000). Hadraoui et al. (2019) investigated the origin of the glycine on 67P/C-G and concluded that glycine is formed in the ice and is subsequently sublimated off where it can be detected.

Previous studies have compared protostars or protostellar models with comets (e.g., Drozdovskaya et al. (2018), Visser et al. (2009)). However, these studies focus on other areas of the system and do not invoke the observations of sputtered material. Drozdovskaya et al. (2018) made a comparison between the 67P/C-G comet and a protostar using heating from the central protostar. Specifically, they studied where the protostar is heating up the ices, and thus measure the molecules as they enter the gas phase from this heating. They find significant agreement between the contents of 67P/C-G and the protostar IRAS 16293-2422 B. They note differences in abundance of OCS and H_2S between the comet and the protostar, and strong agreement in the SO/SO_2 ratio. While the study was insightful in their comparison, the role of heating in this setup raises complications for constraining the chemistry. When the grain is heated, sublimation and heat-activated chemistry happen simultaneously, and the gas-phase composition therefore may not exactly be the same as the original ice composition. Additionally, not all species sublime at the same time as they have different volatilities. It is important that other chemical factors do not influence the chemistry

during desorption (Burkhardt et al. 2019). Heating of the central protostar occurs over the order of 10^4 or 10^6 years, providing ample time for the chemical composition to change. Thus, in this study, we look towards shocks in protostellar outflows to investigate the molecules leaving the ices, while minimizing the amount of thermal chemistry induced. In a shock, the high speed of the collision knocks the species directly off of the ice on a rapid time scale, unlike heating from the central protostar.

2.4. *Goals*

Based on previous studies of the L1551, we can infer that its structure is conducive to the shock conditions we seek to investigate (Fridlund 2016). Thus, we aim to create an inventory of its chemistry in the outflow shocks. Here we combine spatial and spectral analysis to characterize the region. To do this, we investigate the spatial distribution of the different species. We then compare these to protostellar expectations and comet molecular abundances.

In Section 3 we discuss the methods of our study and how we obtain telescope observations, analyze the data through imaging, extract spectra, and make rotational diagrams. In Section 4, we present images displaying the structure of the protostar and the outflow. To initially constrain the morphology of the outflow, we first focus on the most prominent species, CO, and then widen this structural analysis to the other species detected. In the latter half of Section 4, we discuss the results of extracting a spectra in the central region and identifying the lines. We sort species by chemical family. We then follow with how the spectra compare and differ for different regions along the outflow. Finally, we conclude the results section by discussing how the rotational diagrams reveal the characteristics of the different regions. In Section 5, we present our comparisons to comets and other outflows with potential implications and goals for future study.

3. METHODS

In this section, we begin by describing the telescope used for our observations and its benefits in our project. Next, we address the observations used in this thesis and the subsequent image processing. We extract spectra from the image cubes and identify the carriers of the most prominent spectral features. We then use rotational diagrams to obtain abundances and temperatures to study the overall structure of the region.

3.1. Millimeter Interferometry

For our observations we use the Atacama Compact Array (ACA). Completed in 2013, the ACA consists of four 12-meter, and twelve 7-meter dishes. As an add-on to the overall ALMA array in Chile, the compact array offers unique advantages. The antennas are closer together and shorter than the main array of ALMA and is therefore able to resolve larger spatial structures. This is beneficial to view our target which spans a large scale of ~ 1.5 pc. It can be used in concordance with the overall ALMA array to clearly resolve small angles and still image a large region.

The angular resolution of a diffraction-limited telescope scales with the wavelength observed and the inverse of the telescope diameter as in Equation 2.

$$\theta = 1.22 \frac{\lambda}{D} \quad (2)$$

In Equation 2, θ is the angular resolution of the telescope, λ is the wavelength, and D is the diameter of the telescope. Therefore in working with long wavelengths, one would need a much larger diameter to have a small θ and thus high angular resolution. Therefore observing in the radio would require 100-meter sized dishes (Condon & Ransom 2016). To combat this limitation, we can increase the effective diameter of the telescope by using interferometry. A radio interferometer is a group of

antennas whose signals are correlated to simulate a single telescope of much larger size. Each pair of dishes is separated by a baseline vector. Because of this distance, there is a geometric delay where light waves from an astronomical source lag between antennas. The time lag creates offsets in phase of the signal. Using a Fourier Transform, this can relate the phase differences to reconstruct the differences in emission brightness across the sky. The variation in brightness produces an image of the source at an angular resolution related to the largest baselines. In radio astronomy, we describe our observation with beams. A primary beam is the power pattern of the individual antennas and determines the total region that the radio telescope will be sensitive to. The synthesized beam describes the smallest angular scale that can be resolved in the image and is related to the longest antenna baselines.

3.2. *L1551 Observation*

The observation was taken as a part of the SMORES PROJECT: Shocked Molecular Outflow Across a Range of Environments Survey. The 50 GHz of spectrum span from 292.67 to 361.00 GHz and were broken into six separately observed spectral setups. The source is observed in ALMA band 7 at an RA of 04:31:34 and dec of +18:08:04.9. Ten antennas were used in a 7 meter array with baselines ranging from 8 to 48 meters. We obtain a primary beam for the different segments based on the relationship in Equation 2, using the average wavelength of the segment. The data was calibrated using the ALMA CASA Data Reduction Pipeline. IRAS_04166+2706 was used in atmosphere and WVR calibrations. J0522-3627 was used in atmosphere, bandpass, flux, pointing, and WVR calibrations. J0510+1800 was used in atmosphere, phase, and pointing calibrations. Table 1 summarizes the breakdown of the six spectral setups and their characteristics.

3.2.1. *Imaging*

The interferometric data is configured in the form of three-dimensional spectral image cubes. These cubes indicate the photon flux for two spatial dimensions (RA and Dec) and for the frequency dimension. To begin the analysis, we examine the image cubes in CASA. CASA is a radio astronomy software developed by an international consortium of scientists based at the National Radio Astronomical Observatory (NRAO), the European Southern Observatory (ESO), the National Astronomical Observatory of Japan (NAOJ), the Academia Sinica Institute of Astronomy and Astrophysics (ASIAA), the CSIRO division for Astronomy and Space Science (CASS), and the Netherlands Institute for Radio Astronomy (ASTRON) under the guidance of NRAO.

Using the CASA viewer tool, we can analyze each image of our data cubes individually, as well as view the spectra at any given position. Figure 4 depicts L1551 IRS5 showing flux from CO emissions

Frequency Range [GHz]	Velocity Resolution [km/s]	Angular Resolution [arcsec]	Integration Time [hr]	Primary Beam [arcsec]
292.67-308.52	1.9	4.02	0.4	35.9
296.41-312.26	1.9	4.02	0.5	35.4
300.15-315.99	1.9	3.86	0.4	35.0
337.67-353.52	1.7	3.48	0.5	31.2
341.45-357.26	1.6	3.53	0.5	30.8
345.21-361.00	1.6	3.42	0.5	30.5

Table 1: This table summarizes the characteristics of the observations as broken down into the 6 spectral setups as separated by frequency range including velocity and angular resolution, the integration time, and the primary beam size.

at 3 different ranges of frequencies around the CO J=3-2 transition. The frequencies were chosen to best show the redshifted and blueshifted material flowing out from the center. Specifically, we chose these reference points for the left two panels based on the frequencies of the double peak in the central region spectra of CO. The third panel was chosen as a point of reference for an upper bound on a frequency displaying a CO feature.

The emission from a single species is spread out over multiple frequencies because of the Doppler shift caused by the motion of the material. In addition to the overall movement of the object relative to the observer, matter is moving within the region. To identify lines in the spectra, we must take into account the source velocity. Similarly, the internal motions need to be accounted for in the line width.

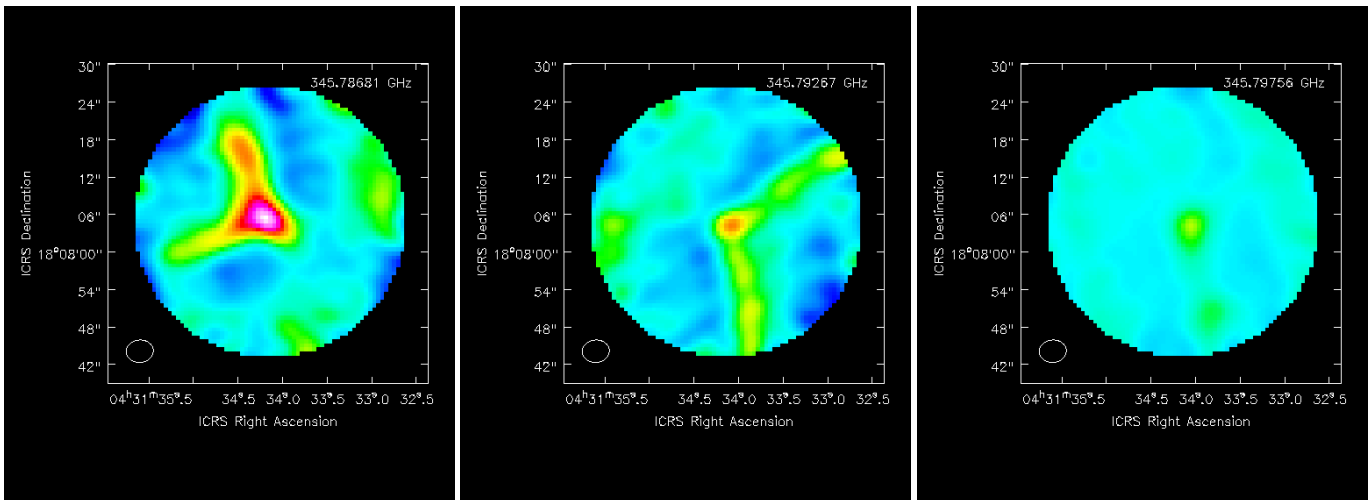


Figure 4: This figure depicts the flux in two spatial dimensions for three different frequency ranges where we expect to see emission from CO. From left to right, the panels depict emission centered at 345.786 GHz, 345.792 GHz, and 345.797 GHz

One advantage of spatially and spectrally resolved observations is that we receive a flux value for each spatial point within our image, and for each spectral channel in the frequency range observed. These points create a three-dimensional image cube with two spatial dimensions (RA and Dec) and a frequency dimension. One way to analyze image cubes is to create moment maps, which collapse a cube into a single image. One common moment map is the moment-0 map where flux is integrated over a range of frequencies in the spatial dimension. This method is useful in understanding the total flux in a region over a range of frequencies. Another map of interest is the plot of the maximum flux at each location by extracting the maximum in each pixel over the range of frequencies. While the maximum flux maps are not used to properly display a measure of brightness, they highlight the overall structure of the object in question. Moment-0 maps are great at showing the structure of the region, and can depict the physical amount of integrated flux over the width of the spectral feature in the region that can be used in further analysis. Maximum maps provide more visual information

to intuit the maximum emission across the frequencies. To create the best image, we must choose a good range of frequencies over which to perform these functions. Originally we used the spectra and estimated one standard deviation away from the peak, but that was adding in additional noise to the image so instead we set the end points based on visual inspection from where a flux at the frequency is present.

3.2.2. Making Spectra

Another way to collapse the spectral image cube is to extract a spectral profile which collapses the spatial dimension of the data. A spectrum is a snapshot at a given location of the flux as a function of frequency. Spectral data is crucial in identifying and determining the abundances of different molecules. The peaks at different frequencies correspond to known transitions for specific molecules. Specifically, radio frequencies probe the rotational transitions. When these transitions occur, molecules fall to a lower rotational energy state by releasing a photon at a particular frequency corresponding to that transition (McGuire et al. 2016).

To extract information on the chemical composition, we can create spectra to examine the flux emitted at different frequencies and locations. From the three-dimensional image cube, we isolate a specific location. To do this, we can work with a specific region over the cube. This region is set to the dimensions of the beam, 2.1 by 1.6 arcseconds and rotated at an angle of -83.4 degrees to match the synthesized beam at the highest frequency of our observations (359 GHz). Using this region, we extract spectra from different locations within our source. We start by defining the central region of the X feature where the center of the protostar resides. To mark this center, we based it on the SO line at 346.5 GHz as it is not an overly abundant feature nor is it displaced significantly from center. It would be challenging to mark the center with CO as it is abundant throughout the X and has a complex kinematic pattern. With the central region established, we then position four masks along each of the four CO outflow features. Together these capture the majority of the structure. Figure 5 shows these 17 regions plotted together over the maximum map for CO.

With these established regions, we extracted full spectra across the frequencies of the survey. Using the CASA `IMVAL` function, we extracted a flux value in Jy/beam for each frequency. For the strongest

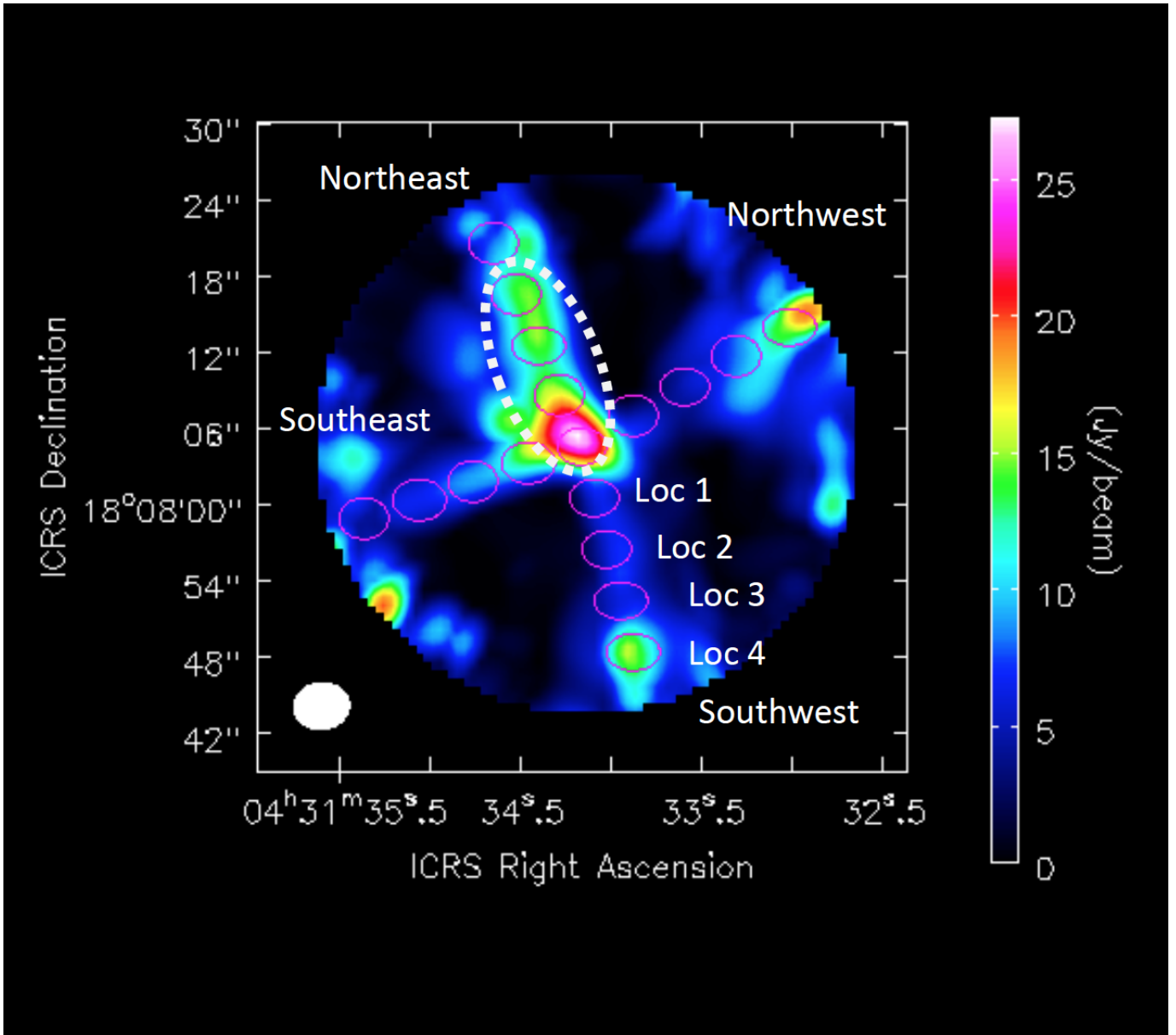


Figure 5: CO maximum map with the 17 regions outlined in magenta. White filled-in oval in bottom left shows synthesized beam. Four branches labeled by relative cardinal orientation. Locations 1-4 are labeled extending out radially and follow this pattern along all four branches. White dashed oval shows the four regions of highest focus in this study: center and northeast locations 1-3.

lines and molecules of interest, we performed a more in depth qualitative comparison on the specific distribution throughout the region. In our analysis, we focus on the center and three inner-most

locations along just one of the four outflow branches. Our methodology to focus in on these regions will be discussed in more detail in the results section.

3.2.3. *Analyzing Spectra*

To analyze the spectra, first we correct the frequency data for the overall movement of the protostars. To correct for this, we use VLSR, the velocity of the local standard of rest to the object. Here we adopt a constant VLSR of +6.5 km/s (Wu et al. 2009). Using this correction, we then identify lines in the central region using the Splatalogue reference catalogue which contains a reference of established molecular transitions with their properties such as upper energy levels. Specifically, we rule out transitions with excitation temperatures greater than 250 K as it would be unlikely for these to be the brightest lines in this source. Once we narrow the range of frequencies, there are often several possible molecular transitions corresponding to the frequencies of the spectral feature. Therefore, we use the energy levels of the transitions to rule out unlikely features. Additionally we compare expected species with literature to check the validity of our identified lines.

After we established a list of molecules, we then used the CASSIS software to help confirm the transitions by fitting the lines. CASSIS (Centre d'Analyse Scientifique de Spectres Instrumentaux et Synthétiques) is a software that has been developed by CESR/IRAP since 2005. It uses SSAP (Single Spectral Access Protocol) to access the IVOA (International Virtual Observatory Alliance) services in order to retrieve any spectra such as Hubble, Corot, Splatalogue, and ISO. We then repeat this identifying process for the 16 regions along the outflow, leveraging central region findings to match the transitions.

With our spectral features identified, we can extract integrated intensities. Using CASSIS, we fit gaussian curves to the peaks in the spectra and integrate the area underneath to evaluate the

integrated intensity (measured in Jy/beam km/s). These value can be used for relative comparisons in abundance. Figure 6 depicts an example of how we use CASSIS to fit the spectral curve and the corresponding area that represents the integrated intensity. We summarize the strongest transitions used to calculate integrated intensity in Table 2 and report integrated intensity values in Table 3. However, for more detailed chemical comparisons, these integrated intensities are converted into column densities. To do this, we can use rotational diagrams and the partition function as described in Section 4.4 of the results.

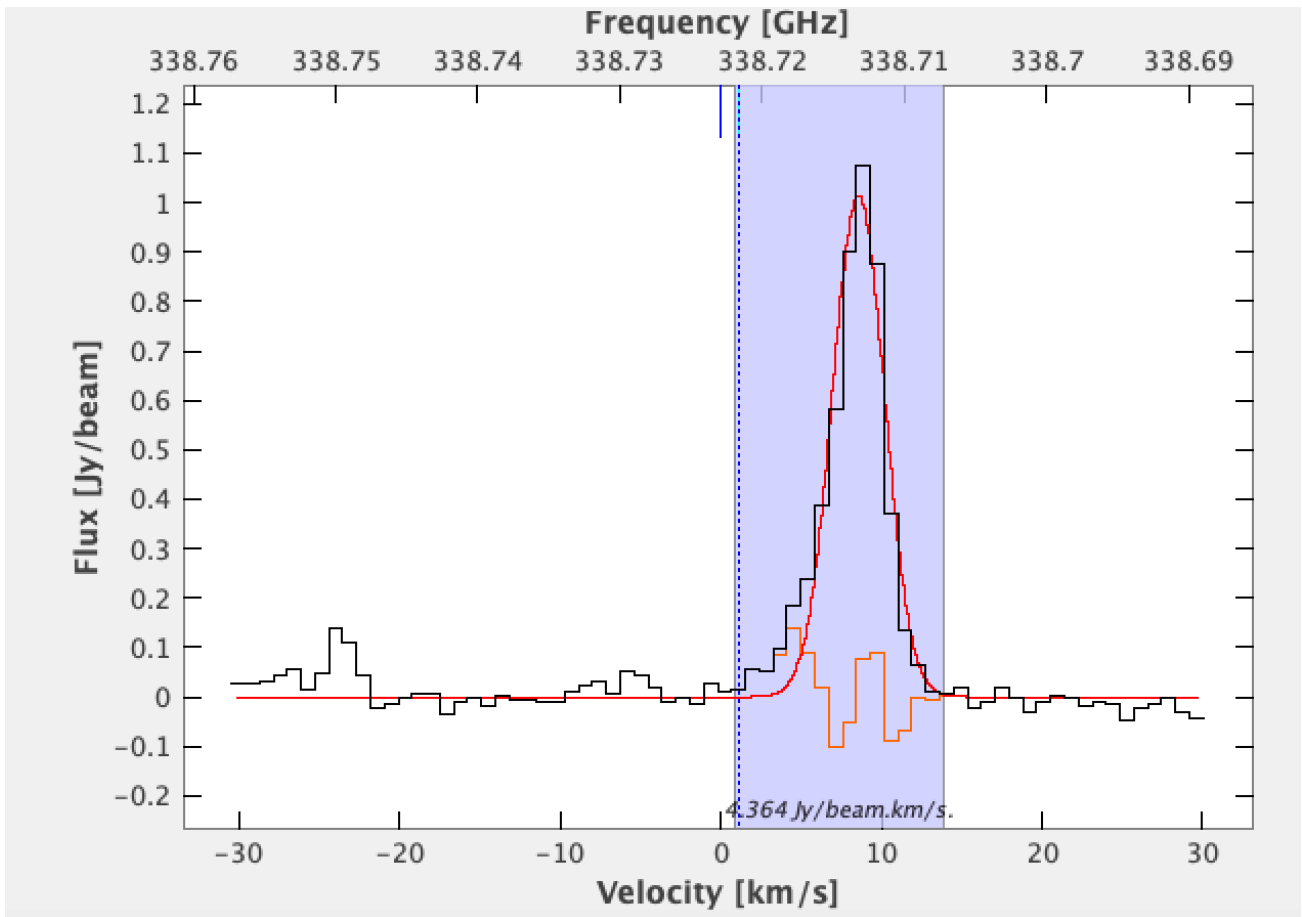


Figure 6: Example of using CASSIS to fit a gaussian curve to a spectral peak. The software extracts an equation of this fit and we use that to calculate the area under the curve. This example depicts the central region spectra from 338.76 to 338.69 GHz, corresponding to the methanol $7_{2,0}-6_{2,0}$ transition.

4. RESULTS

4.1. *Structure of Outflow*

To analyze the structure of CO in the region, we created integrated intensity maps for both the redshifted and blueshifted components of the CO-emission. Here, the contour map (Figure 7) depicts the four branches of the X shaped outflow with the blueshifted outflows on the west (right side) and redshifted materials on the east (left hand side). We find that the data is cleanest and most abundant in the northeast branch. Additionally, there is material on the outskirts of the branches in the opposite color as the main branch. This may suggest that the signal in outermost location (location 4) of the branches could be coming from noise or some other confounding signal. This is likely due to the edge-effect of our observations. Because of this, we decide not to focus heavily on location 4 in our analysis in later tables and the discussion section.

In our source, we see the outflow branches ejecting material away from the center of the protostar. These features are seen prominently along the X structure as material in the two eastern branches (left side of region) is seen at a lower frequency than the material in the western branches. This demonstrates that eastern material is redshifted and moving away from the observer and the emission from CO in the western branches is blueshifted as the material moves towards us. Between the redshifted and blueshifted CO, we see a difference of about 5.86 MHz or 5 km/s.

The shape of the structure in Figure 7 is consistent with the structural study by [Wu et al. \(2009\)](#) (c.f Figure 3). We examine the J=3-2 CO transition which is similar to their findings studying the J=2-1 CO transition. The X shape depicted coincides with the limb brightened walls of the outflow as we are looking through more material at these locations. The angle of the opening and spread of CO of this cavity is comparable to that in the Wu study. As CO is the brightest line, and is expected

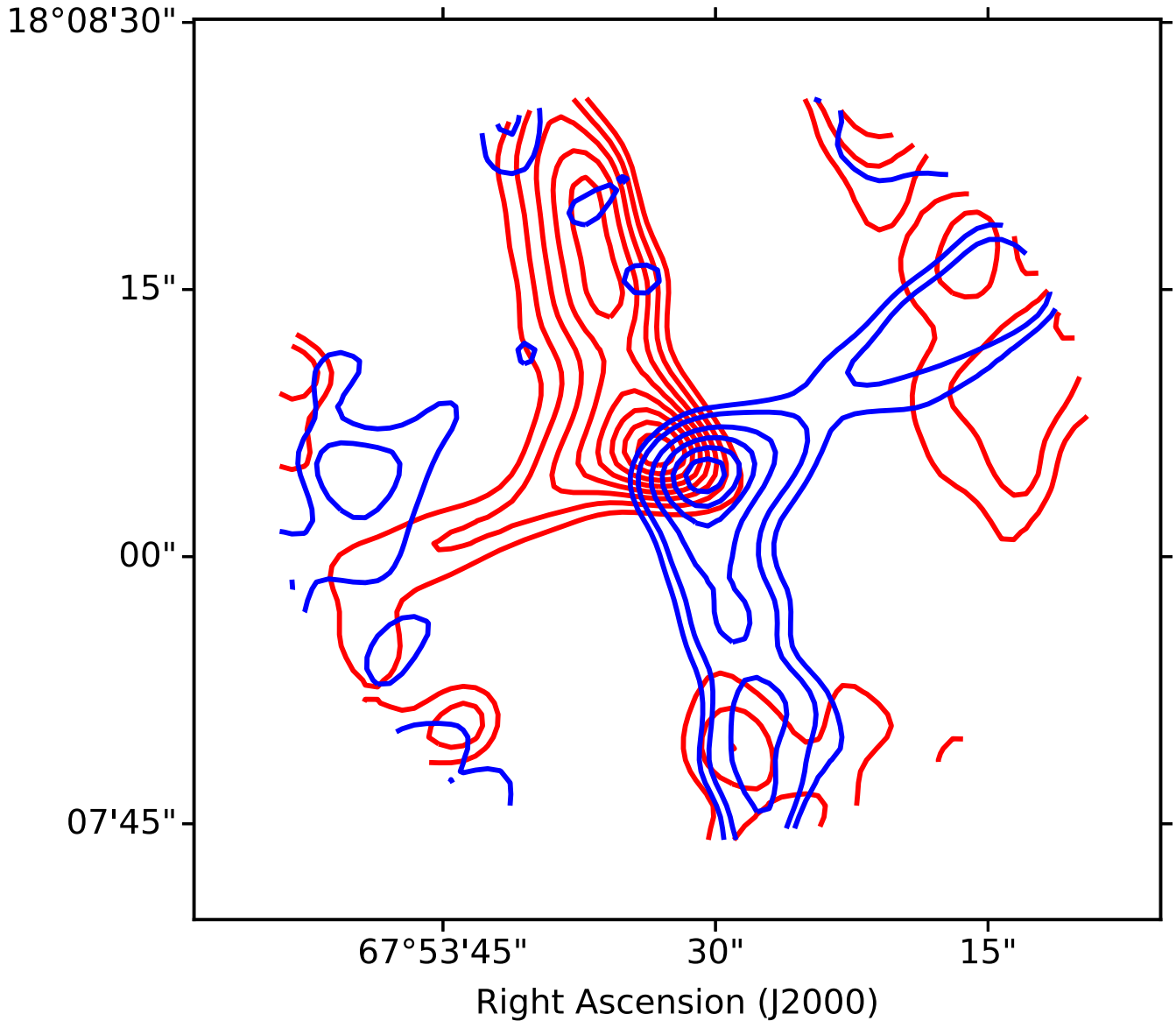
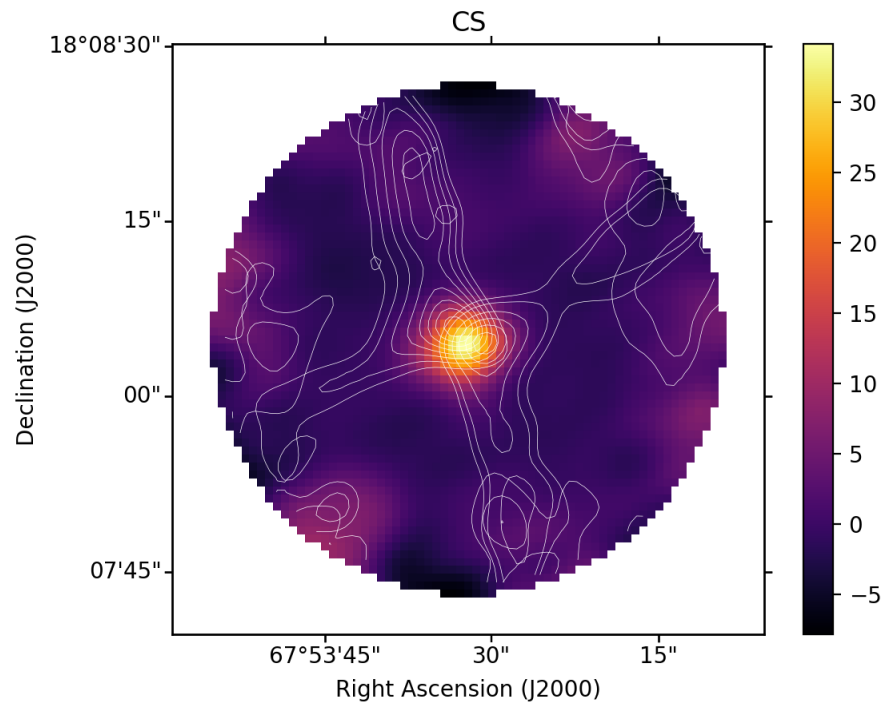
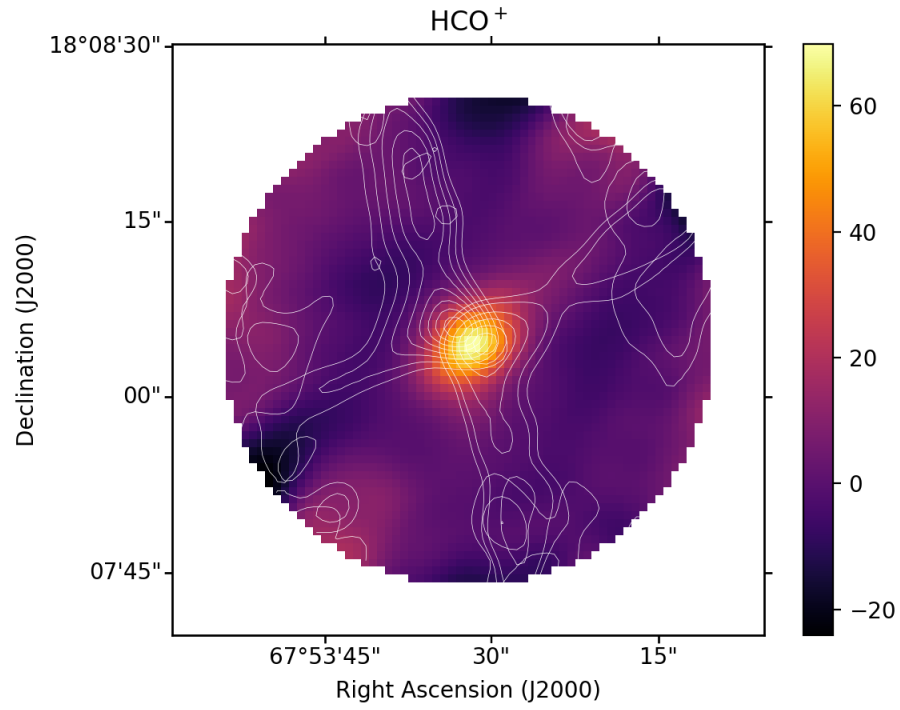


Figure 7: Moment-0 map of CO structure from the J=3-2 transition centered at 345.80 GHz. Red contours label flux measured at frequencies lower than 345.80, and blue contours correspond to higher frequencies. The outermost contour starts at 5 Jy/beam, then goes up to 10, followed by steps of 10 Jy/beam up to a maximum of 80 Jy/beam in the center contours.

to be abundant throughout the structure, it is a good probe for the overall physical structure of the region.

We then overlay these two moment maps to show the structure of the outflows ejecting other material out from the central protostar, as seen in Figure 8. With the dominant CO structure outline, we can then compare the structure of other molecules. Specifically, in our next step of analyzing the structure, we compare the structure of CO to the distribution of the formylionium (HCO^+), carbon monosulfide (CS), sulfur monoxide (SO), and formaldehyde (H_2CO). Figure 8 depicts the CO contours from Figure 7, overlaying the moment-0 maps of these other four species.

Figure 8 shows that for HCO^+ , CS, H_2CO , and SO the majority of material is concentrated to the center. We see that each species has some presence flowing out from the central region. However, this emission is much weaker than seen at the center. Thus by visual inspection, it appears that the majority of these species are concentrated to the center. Faint tracings, however, can be seen along the outflow. The flux is several factors lower in the outflow regions. To interpret whether these features beyond the center protostar are real, we proceed to do a qualitative analysis along the branches. In the following section, we will explore the column densities along the outflow to evaluate the presence of these species in the northeast branch. Looking at Figure 8, we recognize the circular pattern of noise as the edge effects of the beam. This pattern is particularly noticeable in the SO panel and solidifies our decision to rule out location 4.



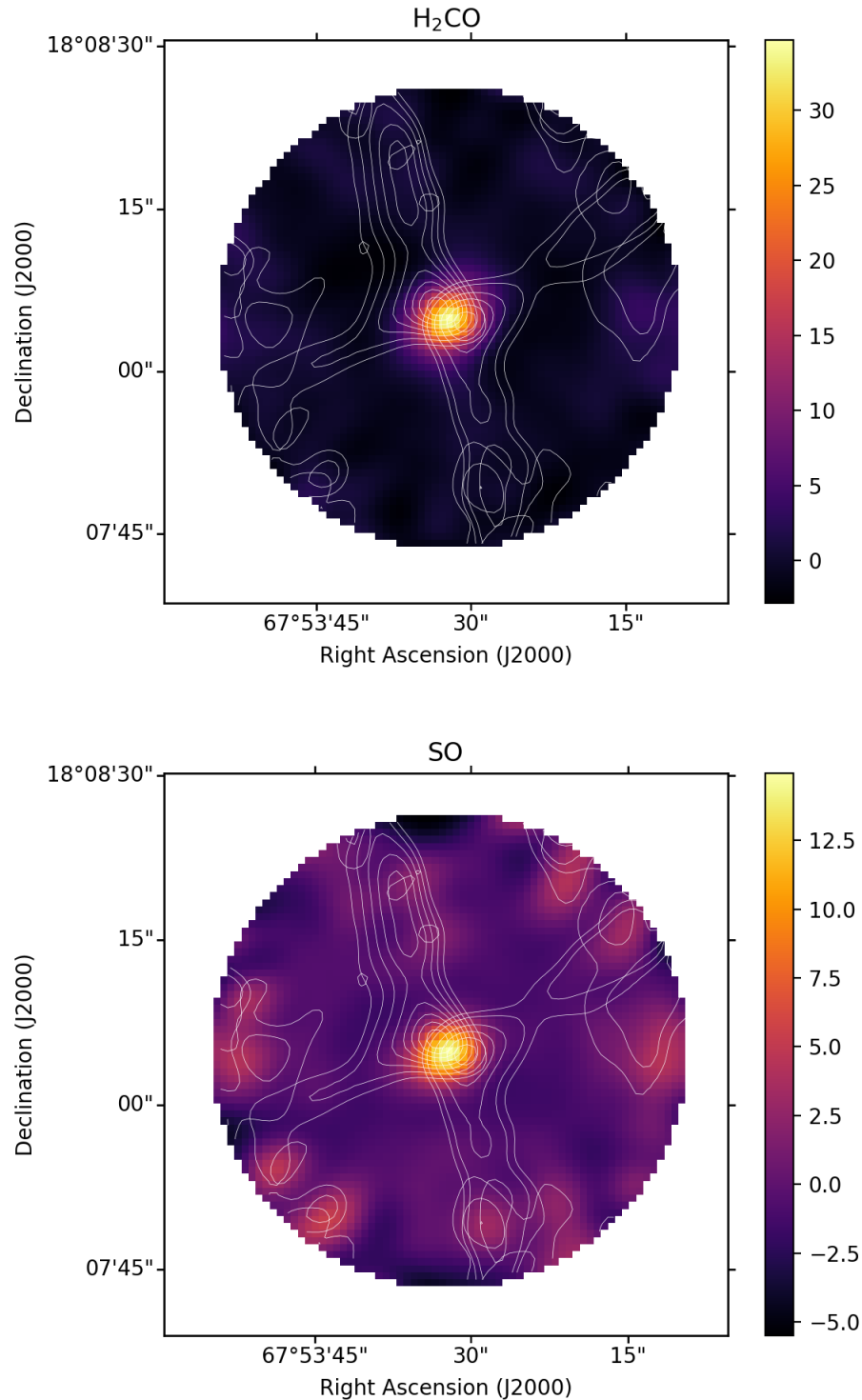


Figure 8: Moment-0 maps of flux [jy/beam] as a comparison to CO outflows. White contours overlay the CO distribution with the same scale as Figure 7. Transitions of each molecule correspond to the frequencies of the largest spectral feature at frequencies and transitions reported in Table 2. The top panel corresponds to HCO^+ and the second panel shows CS. The third panel depicts an H_2CO transition and the bottom panel depicts SO emission.

4.2. *Line Identification*

The central region of the protostar is where we see the richest chemistry due to the higher temperature and density of the region. Thus we expect to see the brightest and largest number of lines toward the central region. Figure 10 depicts the spectra of the central protostar.

Indeed, in Figure 10, we see a clear range of different molecular transitions, including some absorption features. The negative feature is most prominent with CO where the high density means there are more molecules present to absorb CO photons at that Doppler shifted velocity than there are emitting a photon at that transition frequency. We also see these small negative adsorption features on other lines. Absorption features are mostly seen in the brighter lines as the material is more dense, such as with CO and HCO⁺. We also see that some species have multiple lines corresponding to multiple transitions at different regions. Here, we identify the brightest transitions in the spectra toward the protostar and use these lines as a template for spectra occurring in the branches.

Based on the central region spectra, we can determine the transitions present for each species and the characteristic of those transitions. Table 2 summarizes the nine most prominent species, including the number of lines and strongest transition for each molecule. The most prominent lines in our central region spectra correspond to CO, CS, SO, SO₂, HCO⁺, H₂CO, CH₃OH, HCN, and CN. We estimate that we have identified about half of all the features present. These molecules are all reasonable to expect in protostars with transitions corresponding to appropriate upper level energy states (Boogert, et al. 2015). In the central region, CO is by far the brightest. We also see that species such as SO₂ and CH₃OH, have significantly more identified lines and have peaks with lower flux. Additionally, these species can be grouped into families of chemically related species such as organics, sulfur bearing molecules, and small species. From preliminary inspection of species-family

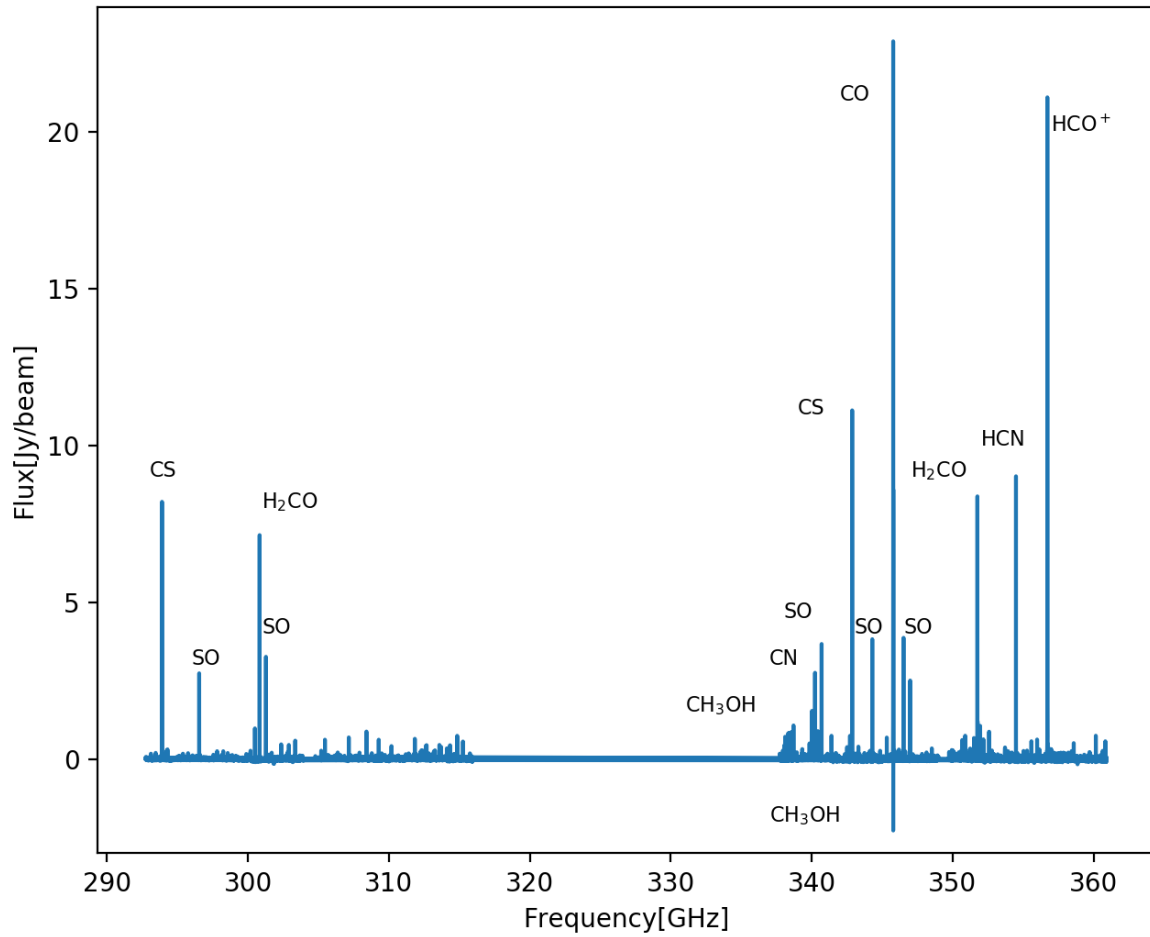


Figure 9: Spectra of central region with labeled transitions. The brightest peak corresponds to the CO line. At the CO transition, there is a negative feature at 345.8 GHz from the absorption. HCO⁺ is the second strongest line in the central region. There are no lines with flux above 10 Jy/beam in the frequency segments below 315 GHz. We used the SO transition to the right of the CO line to center our region. SO, H₂CO, CS, and CH₃OH all show multiple strong peaks. CH₃OH features come in clusters with many smaller peaks close together.

Molecule	Number of Lines	Flux of Strongest Line [Jy/beam]	Main Transition	Frequency [GHz]
CO	1	22.90±1.42	3 - 2	345.80
CS	2	11.13±0.21	7 - 6	342.88
SO	8	3.87±0.15	9 ₈ - 8 ₇	346.53
SO ₂	15	0.69±0.04	13 _{2,12} - 12 _{1,11}	345.34
HCO ⁺	1	21.12±1.34	4 - 3	356.73
H ₂ CO	2	8.38±0.11	5 _{1,5} - 4 _{1,4}	351.77
CH ₃ OH	36	1.07±0.06	7 _{2,0} - 6 _{2,0}	338.72
HCN	1	9.02±0.21	4 - 3	354.51
CN	19	2.76±0.23	3 _{0,2.5,4.5} - 2 _{0,2.5,3.5}	340.25

Table 2: Summary of the nine species of focus with their corresponding number of identified lines. Additionally, the strongest spectral feature for each species is recorded with its corresponding flux, transition, and frequency. Error on flux stems from the fit of the curve as exemplified by the gaussian in Figure 6.

comparisons, there is no apparent trend in abundance. We will return to familial trends in the discussion section with respect to their spacial distribution throughout the object.

4.3. Molecular Emission Across outflow

4.3.1. Distribution of Carbon Monoxide

We now compare species by spatial distribution. Figure 10 demonstrates how we extracted spectra at each of the 17 regions highlighted in magenta ovals. Specifically, here we zoom in on the spectra of four regions centered around the CO transition. Comparing the CO line profiles from four of these positions, we see variations in CO emissions between the four branches. The strongest signal of CO is seen in the northeast branch, and thus we decide to proceed to only consider this branch as the representative outflow.

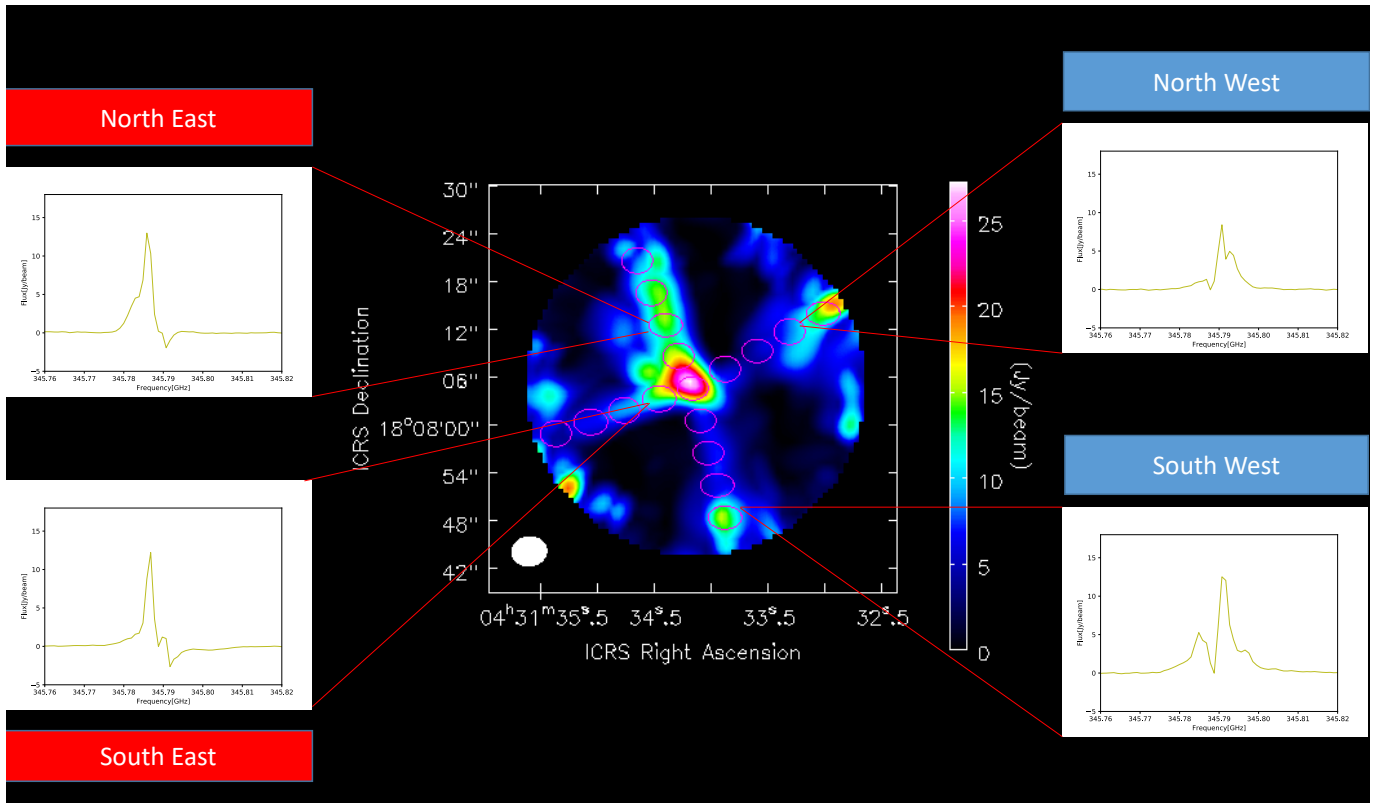


Figure 10: Four sample spectra of CO corresponding to four different regions across the different outflow arms.

We then can compare the spectra for each of the regions. To closely examine the distribution of CO, we zoom in at the spectral features from 345.76 to 345.82 GHz in Figure 11, centered around the J=3-2 CO peak.

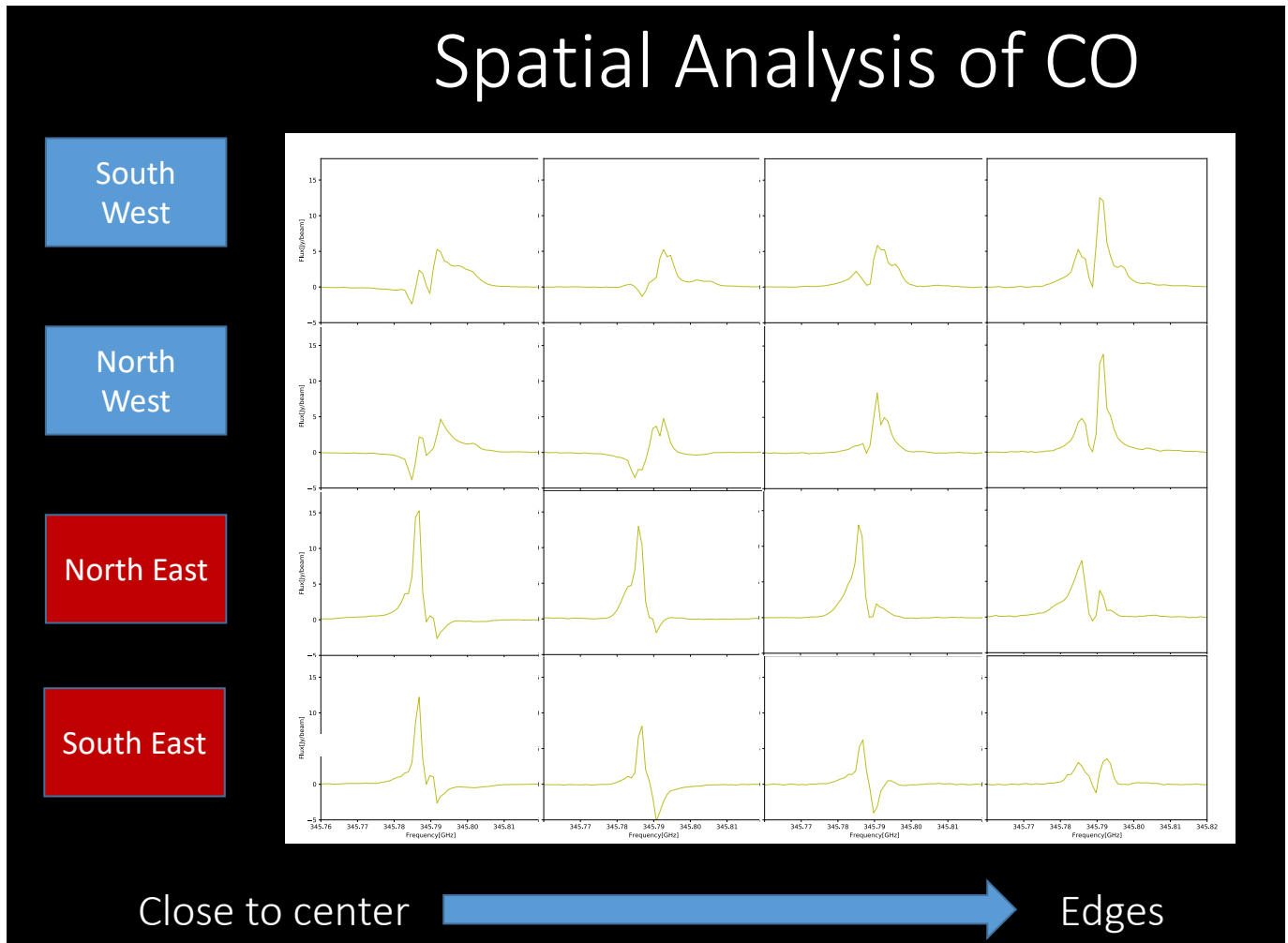


Figure 11: Spectra of CO distributed throughout the 16 outflow locations. From left to right, the spectra move out radially from the central region. Negative flux corresponds to absorption features. Rows show the different branches.

Looking close in on the spectra in Figure 11, we can see there are distinct variations in the CO emission across the different regions of the object. There is pronounced redshifting and blueshifting

of the material, with western lines peaking at higher frequencies than those in the two western branches. However, there are not shifts in the dips in the spectra. This demonstrates that these are absorptive features of ambient material in front of the outflows, and is not moving towards or away from us at high speeds as the outflow is. A clear example of this is seen in the dip around 345.788 GHz, constant in both the western and eastern regions. Additionally, we can learn about the spatial distribution of CO. A point of interest is the difference between the western and eastern outflows. In the western branches, we see the emission from CO increases with increasing radial distance from the center, while in the eastern branches, emission from CO decreases as a function of radial distance from the center. This suggests some asymmetry in the distribution along the outflow or perhaps in our observations.

4.3.2. *Integrated Line Emission for Prominent Species*

As discussed in methods, we calculate integrated intensities throughout the protostar. Table 3 summarizes integrated intensities for the main transitions (Table 2) at the center protostar and the three positions extending radially outward in the northeast branch. This also includes the corresponding upper energy and $S\mu^2$ values that are used in calculating the column density.

Here we examine more qualitatively how HCO^+ , CS, H_2CO , and SO vary as they extend radially outward from the central protostar as shown in Figure 12.

It is important to note that we do not calculate integrated intensity from absorption features and thus are not plotted in this figure. Thus a missing point on the graph can correspond to an absence of a molecule, or it is present as absorption. In Figure 12, there is a steep dropoff in the integrated intensity from the center of the star to location 1 along the branches, and again between the first two regions of outflow along the branches. We also see that the different species behave differently as a function of radial distance from the center. For example, SO does not appear to fall off as quickly, and in fact sees a large spike at the outer edge of the outflow. HCO^+ and CS also see some small increases again at location 4 at the edges of the branches. In comparison to the central region, H_2CO maintains the largest percent of intensity in the outflow from the central region. Then CS and HCO^+ maintain a fair percent of intensity from the central region of CS. SO falls off by nearly an order of magnitude from the center to the 1st step of the branch, but still picks up again in location 4. We also see distinct patterns of variation between the different branches. For example, the northeast branch tends to have lower integrated intensities of all these species. We see similarities within the sulfur bearing species in terms of the shape of the curve in Figure 12, but in future work we would like to expand this to include more species to evaluate trends of distribution by chemical family.

Molecule	E_u (K)	$S\mu^2$	$\int Tdv(\text{Center})$	$\int Tdv(\text{Loc. 1})$	$\int Tdv(\text{Loc. 2})$	$\int Tdv(\text{Loc. 3})$
	[K]	[D ²]	[Jy/beam km/s]	[Jy/beam km/s]	[Jy/beam km/s]	[Jy/beam km/s]
CO	33.19	0.04	111.48±29.72	33.84±0.06	33.68±6.35	37.85±7.48
CS	65.83	26.99	20.86±0.75	6.18±0.24	0.02±0.21	1.12±0.16
SO	78.78	21.53	10.96±0.64	0.39±0.53	0.27±0.30	0.17±1.95
SO ₂	92.98	13.41	3.13±0.18	—	0.03±006	—
HCO ⁺	42.80	60.45	70.39±6.72	7.99±1.41	—	1.61±0.35
H ₂ CO	62.45	78.23	22.78±0.47	4.86±0.17	0.44±0.09	1.74±0.16
CH ₃ OH	86.26	5.14	3.86±0.33	0.11±0.08	—	0.03±0.06
HCN	42.53	35.90	29.32± 0.99)	3.60±0.14	—	0.38±0.16
CN	32.67	4.81	9.34±1.10	2.15±0.20	—	1.25±0.12

Table 3: Integrated Intensity of strongest transition in northeast branch in Jy/beam km/s with corresponding upper energy of the transition. These transitions correspond to the lines at the same frequency in Table 2. For regions with dashes, features are either seen in absorption or the line is not detected. The $S\mu^2$ values were acquired from the JPL data in Splatalogue. The upper level energies were acquired from CASSIS. Errors reported indicate the error on the fit of the spectra and the noise of observation. Integrated intensities for regions along other branches and the errors on the integrated intensity calculations can be found in Table 7 in the Appendix. Locations 1, 2, and 3 refer to the locations denoted in Figure 5 along the northeast arm.

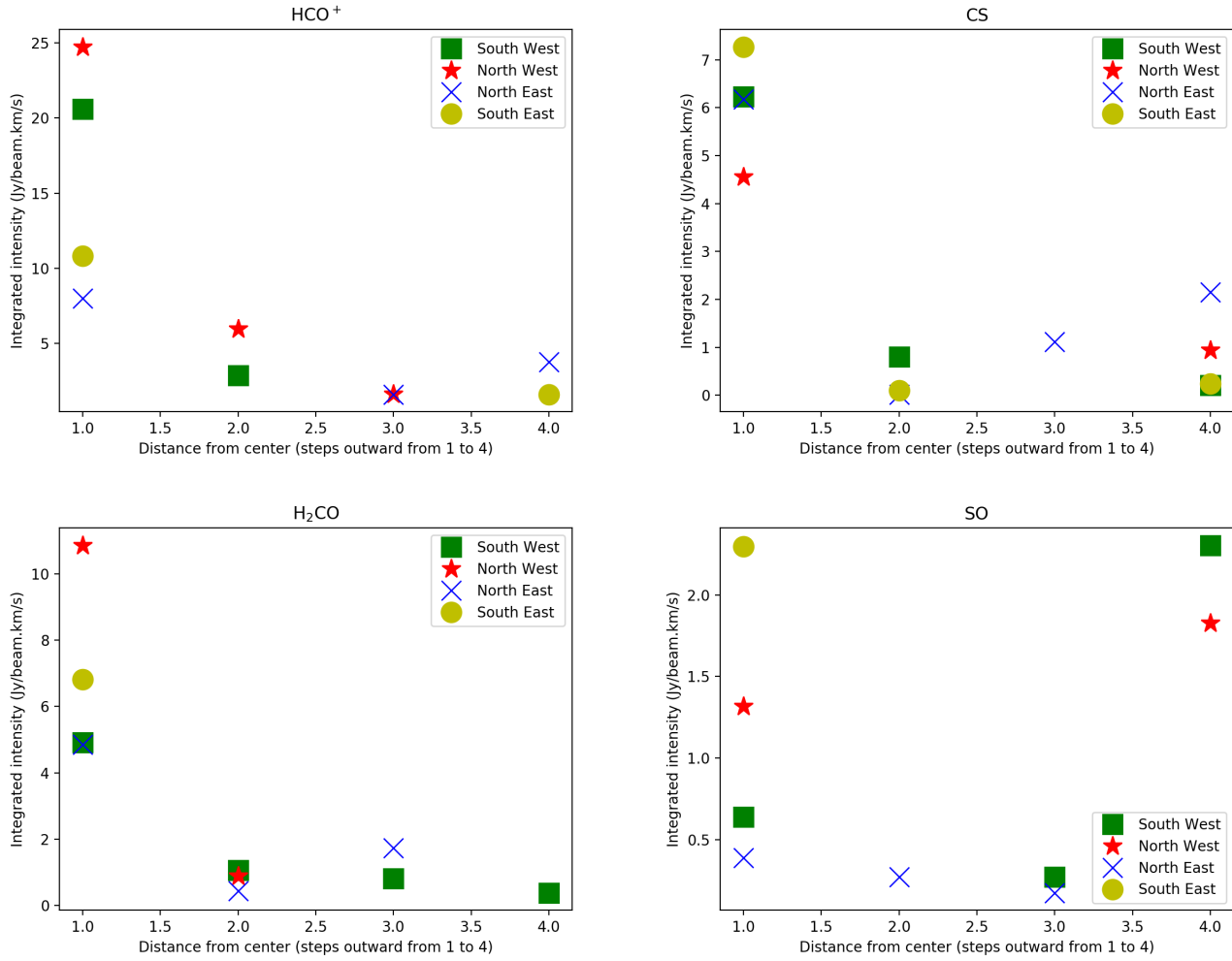


Figure 12: Integrated intensities as a function of radial distance from the protostar in increments of 1 to 4 representing the four spatial steps along the X of the outflow. Colors/shapes indicate the outflow branch. Top left: HCO⁺, Top right: CS, Bottom left: H₂CO, Bottom right: SO. Missing data points represent absorption lines which we did not consider here.

4.4. *Extracting Abundances and Temperature with Rotational Diagrams*

By integrating under the spectral peaks for multiple transitions of the same molecule, we are able to extract physical properties. The differences in the energy levels of the transitions allow us to utilize rotational diagrams. A rotational diagram plots the upper energy (E_u) by $\ln(\text{Nu}/g_u)$. Previous studies have related these two quantities through a linear fit of Equation 3 (Blake et al. 1987) :

$$\ln\left(\frac{3kc \int T_b dv}{8\pi^3 \mu^2 v^2 S}\right) = \ln \frac{N_T}{Q(T_{rot})} - \frac{E_u}{KT_{rot}} \quad (3)$$

Where N_T is the total molecular column density summed over all the levels, E_u is the energy of the upper transition state, and $Q(T_{rot})$ is the rotational partition function at temperature T_{rot} . The CASSIS software uses this expression as a linear fit to the data to extract a column density for the molecule and the rotational temperature in that region. We then repeat this for all identified molecules with multiple transitions and different regions. Ultimately, these column densities can be related to abundances relative to hydrogen.

Figure 13 is an example of a rotational diagram in the central region. This line was computed using the CS transitions at 342.88 and 293 GHz. From this diagram we find a central region temperature of 249.6 K and column density for CS of $1.4 \times 10^{14} \text{ cm}^{-2}$. In the results section, we will provide a comprehensive representation of all the rotational diagrams used in this study. For several regions, absorption or non-detections prevented us from having enough lines to create rotational diagrams. Additionally, this method only applies for species that we have two or more transitions at significantly different upper energy levels covered in our range of frequency for the survey. In these scenarios, which we are unable to create a rotational diagram, we use Equation 3 to calculate N_T by assuming a rotational temperature by averaging all rotational temperatures that were able to be fit toward that

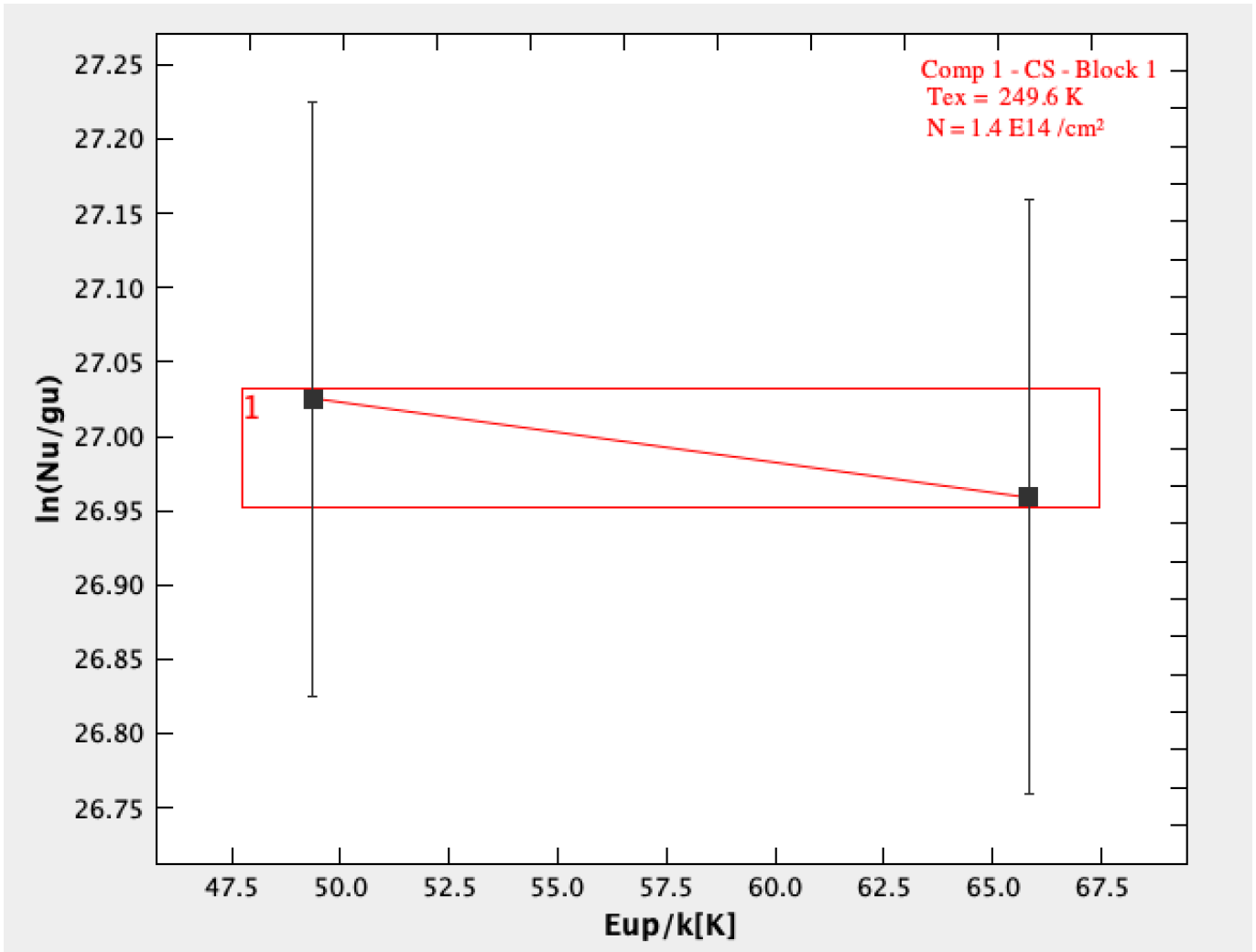


Figure 13: Rotational diagram of CS in central region. The two points each represent a transition in our spectra with a corresponding upper energy (x-axis). Note that upper energy is divided by the boltzman constant for consistency of units. CASSIS produces values for $\ln(Nu/gu)$ on the y-axis by integrating under our spectra and applying Equation 3. Red line indicates regression fit.

region. For the species where multiple transitions existed but with similar upper level energies, we use our strongest transition for the calculation of Equation 3. We use the frequency, upper energy, and $S\mu^2$ value from the Splatalogue database which correspond to this transition. Additionally, we assign a $Q(T)$ value for each region for each species. We extract $Q(T)$ from fitting a logarithmic plot

based on the CASSIS sqlrpartitionmol database for each species. By fitting this plot, we can extract $Q(T)$ and use the value at the assigned temperature in the region. Next, in Equation 4, we use our calculated integrated intensity to calculate the $\int T_b dv$ element of Equation 3, corresponding to the integrated intensity.

$$\int T dv = 1.36 \frac{\lambda^2}{\theta_{min} \theta_{maj}} I \quad (4)$$

In Equation 4, λ is the wavelength (cm), and the two angles correspond to the major and minor axes of the beam in arcsec. I is integrated intensity in mJy*cm/(beam*s). This is then converted to $\int T dv$ to use frequency, not velocity. Thus we have constrained the values to calculate our approximated column density.

4.4.1. Rotational Diagrams across outflows

We expand to obtain column densities throughout the outflow. Figure 15 displays the rotational diagrams for the five species with strong lines corresponding to at least two transitions of two different upper energy levels. We see that species like H₂CO and CS have two lines to use in our survey. Others like CH₃OH and SO₂ have many lines, better constraining the slope of the fit to extract the temperature and column densities. However, it should be noted that methanol is particularly known for creating muddled rotational diagrams because of a complex excitation structure. We rule out points in these plots with high upper energies. Specifically, we eliminate unrealistic points with upper energies an order of magnitude greater than the other points as they likely correspond with confounding spectral features or transitions. Other points that seemed distant from the line were also investigated in more detail to check for confounding signals. It should be noted that location 2 in the outflow appears to give the weakest signal overall as the line is not bright enough to see, suggesting

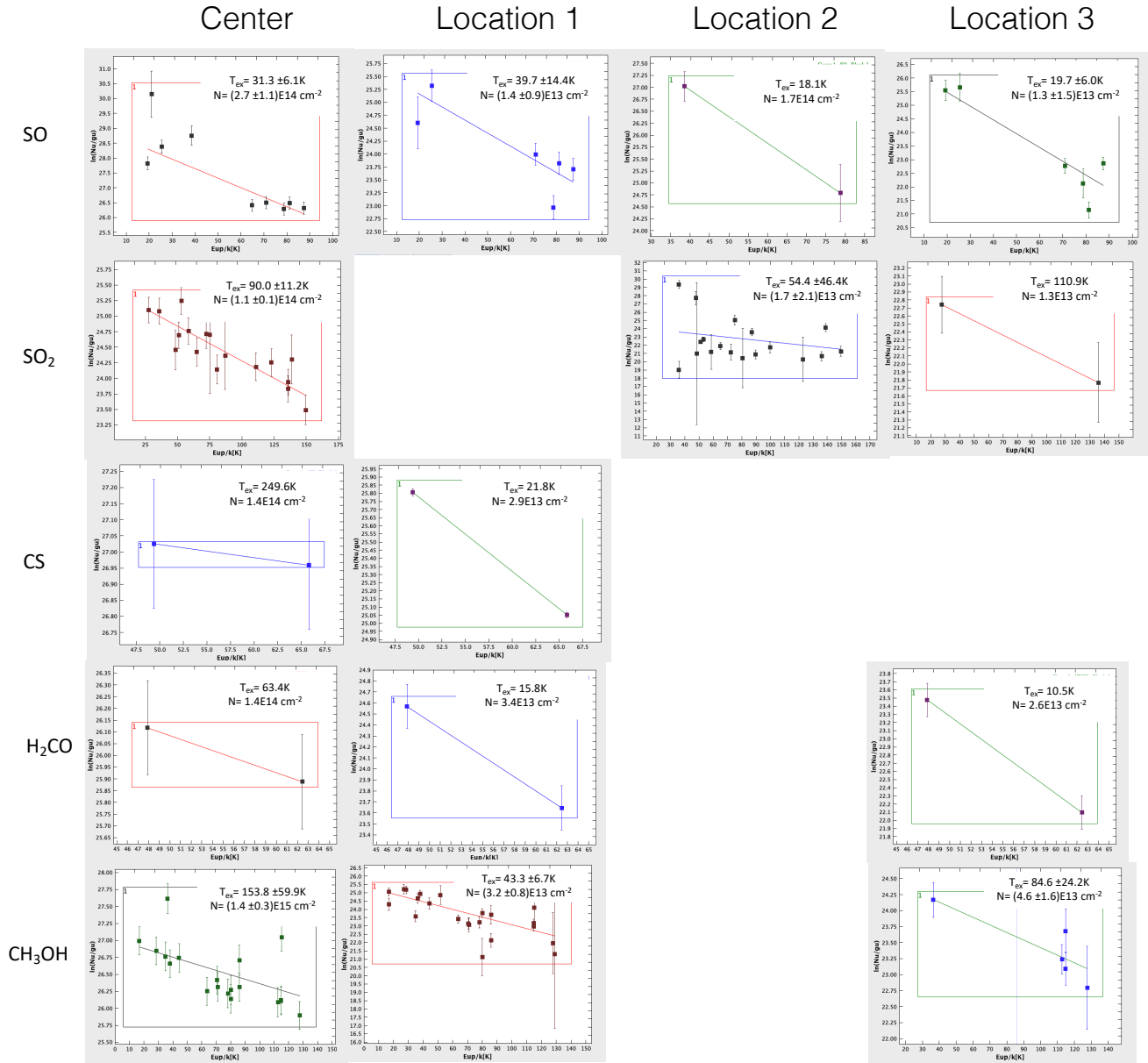


Figure 14: Rotational diagrams with log scale show a linear fit. Empty spots indicate locations where lines are in absorption or complicated by other signals and noise. There is a negative correlation between upper level energy and N_u/g_u . Some plots have more transitions present than others within the species as only clearly identified spectral features were used. Additionally, some points were eliminated based on upper bounds discussed in this section.

Molecule	$T_{\text{rot,Center}}$ [K]	$T_{\text{rot,Location 1}}$ [K]	$T_{\text{rot,Location 2}}$ [K]	$T_{\text{rot,Location 3}}$ [K]
CO	—	—	—	—
CS	249.6	21.8	—	—
SO	31.3 ± 6.1	39.7 ± 14.4	18.1	19.7 ± 6.0
SO ₂	90.0 ± 11.2	—	54.4 ± 46.4	110.9
HCO ⁺	—	—	—	—
H ₂ CO	63.4	15.8	—	10.5
CH ₃ OH	153.8 ± 59.9	43.4 ± 6.7	—	84.6 ± 24.2
HCN	—	—	—	—
CN	—	—	—	—
Average	117.62 ± 86.43	30.18 ± 13.45	36.25 ± 25.67	56.43 ± 49.06

Table 4: Temperatures calculated from rotational diagrams (K) with errors from fit. Row of average temperatures are taken as the mean for the species with standard deviation we were able to extract from.

there is either less of this molecule at that location or there is some difference in the excitation at that location (e.g., the area is colder and thus emits less at that transition).

The diagrams in Figure 14 are used to extract temperatures as summarized in Table 4. We see the warmest temperature in the central protostar, with a clear falloff into the outflow. In location 2, there is insufficient temperature data to see a trend decreasing from region one. Location 3 sees a dichotomy with low temperatures for SO and H₂CO and high excitement temperatures for CH₃OH and SO₂.

Table 4 shows the temperatures extracted from the 15 rotational diagrams. Combining these values with the integrated intensities in Table 3, we then calculate our column densities using rotational diagrams and Equation 3, assuming a temperature for species with one transition. Table 5 summarizes the values of column density in the central protostar and the three locations along the northeast branch in increasing radial distance from the center. This table includes both values taken from our 15 rotational diagrams, and those calculated separately using integrated intensity and an assumed temperature (denoted in table with a tilde). As CO is optically thick, we report here a lower limit on column density. In our calculations, we find that our species fall off between one to two orders of magnitude between the center and the outflow. CN, alone, remains on the same order of magnitude in all positions.

Molecule	N_{Center} [cm ⁻²]	$N_{\text{Location 1}}$ [cm ⁻²]	$N_{\text{Location 2}}$ [cm ⁻²]	$N_{\text{Location 3}}$ [cm ⁻²]
CO	$\geq 2.45 \pm 1.92 \times 10^{18}$	$\geq 5.15 \pm 2.47 \times 10^{17}$	$\geq 5.00 \pm 3.66 \times 10^{17}$	$\geq 5.96 \pm 5.26 \times 10^{17}$
CS	$1.4 \pm 1.03 \times 10^{14}$	$2.9 \pm 1.29 \times 10^{13}$	————	————
SO	$2.7 \pm 1.1 \times 10^{14}$	$1.4 \pm 0.9 \times 10^{13}$	$1.7 \pm 2.23 \times 10^{14}$	$1.3 \pm 1.5 \times 10^{13}$
SO ₂	$1.1 \pm 0.1 \times 10^{14}$	————	$1.3 \pm 0.7 \times 10^{13}$	$3.0 \pm 2.5 \times 10^{13}$
HCO ⁺	$\sim 1.21 \pm 0.89 \times 10^{15}$	$\sim 1.15 \pm 0.55 \times 10^{14}$	————	$\sim 2.10 \pm 1.88 \times 10^{13}$
H ₂ CO	$1.4 \pm 1.03 \times 10^{14}$	$3.4 \pm 1.51 \times 10^{13}$	————	$2.6 \pm 2.27 \times 10^{13}$
CH ₃ OH	$1.4 \pm 0.3 \times 10^{15}$	$3.2 \pm 0.8 \times 10^{13}$	————	$4.6 \pm 1.6 \times 10^{13}$
HCN	$\sim 2.57 \pm 1.89 \times 10^{15}$	$\sim 2.65 \pm 1.18 \times 10^{14}$	————	$\sim 2.54 \pm 2.45 \times 10^{13}$
CN	$\sim 9.90 \pm 7.37 \times 10^{15}$	$\sim 1.55 \pm 0.70 \times 10^{15}$	————	$\sim 9.44 \pm 8.26 \times 10^{14}$

Table 5: Column densities in the northeast branch with increasing position from center and uncertainties noted in parentheses. Tilde corresponds to values calculated assuming an excitement temperatures. Errors on calculated values (with tilde) from propagation error of integrated intensity and average temperature. Note that the error from the noise of the observations is folded into error on integrated intensity. Other values without tilde were found using rotational diagrams. Errors for regions and species with rotational diagrams through three or more points represent error on the regression fit. CO calculations mark a lower limit on column density. Dashes indicate region in which there was not at least one clean transition with a positive spectral feature.

5. DISCUSSION

5.1. *Spatially Resolved Chemistry Along Outflows*

Due to passive heating, we expect a fall-off in concentration with distance from the central protostar. We additionally expect an increase of species that sputter from the ice phase where shocks occur. Table 6 lists our column densities for the central protostar and average of the different outflow regions and compare these with two other protostars, one where molecules were also measured in the associated outflow. Additionally we compare these protostars to comet 67P/C-G. To test the relative spatial abundances of the different species in L1551, we start by comparing with studies of other protostellar outflows. One such study was [Palau et al. \(2017\)](#) who investigate SO and HNC emission along the outflow cavity walls of IRAS 20126+4104 and compare abundances with CH₃OH and CO, and H₂CO. Other prominent lines include H₂CO, and SO.

Apart from CO, [Palau et al. \(2017\)](#) find a lower density in the outflow relative to the disk for the species also analyzed here for L1551 (SO, H₂CO, and CH₃OH). As CO is optically thick, we do not focus on this comparison. We don't resolve the disk in our observations but we assume that it is relevant to compare their disk densities to our central region since our inner region probes a similar physical scale as their disk. We note that they followed similar assumptions in their column density calculations. For SO, they find column densities about two orders of magnitude higher in 20126 than we did in L1551. In terms of dropoff from the center to the outflow, [Palau et al. \(2017\)](#) found a falloff from the center to the outflow by roughly a factor of 2.5. In our analysis of SO, we find a consistent though more prominent falloff in density by a factor of 4.1. Again in H₂CO and CH₃OH we have lower column densities throughout by two to three orders of magnitude. In H₂CO they find a 2.9 times higher density towards the center of 20126. This again compares to a consistent, though

slightly stronger, falloff factor of 4.7. In CH_3OH we find a higher falloff rate again. However, in this case the L1551 rate is significantly higher than that of 20126 where we find rate of 36 compared to their factor of 3.5. From these observations we infer that for the smaller molecules we get consistent decreases between the center and outflows of L1551, but here with these larger molecules the decrease is much more extreme.

Overall, in each of these three species, we are seeing a larger falloff between the central protostar and the outflow of L1551 than that of IRAS 20126+4104. Perhaps this trend could be confounded by having significantly higher densities of these species in the center protostar of IRAS 20126+4104 than L1551. We in part attribute our lower column densities overall to the optical thickness and to the fact that we are not calculating integrated intensity where there are absorption features. These differences can also be impacted by the stage of life and age of the protostar. Additionally, it is interesting to note that for most of their more complex species, such as HCOOCH_3 [Palau et al. \(2017\)](#) they see the opposite trend where column densities are higher in the outflow than in the disk.

To summarize, we see a similar decrease for all smaller species common to both studies, but a much more significant decrease in methanol. Methanol is known to form exclusively on grains, thereby suggesting that the L1551 outflow is either impacting a region poor in CH_3OH or that it has weaker shocks that do not sputter ice mantles as efficiently as in 20126.

Another comparison we can form with IRAS 20126+4104 is the relative abundances of different species to one another. In L1551 we find a ratio of CH_3OH to H_2CO to be 10 in the center and 0.8 in the outflow. In IRAS 20126+4104 this ratio is 450 in the center and 378 in the outflow. We find a larger decrease in this ratio for L1551 than in IRAS 20126+4104. CH_3OH can only form in ice, while

Molecule	$N_{L1551,Center}$ [cm ⁻²]	$N_{L1551,Outflow}$ [cm ⁻²]	$N_{I20126,Center}$ [cm ⁻²]	$N_{I20126,Center}$ [cm ⁻²]	$N_{I16293 B,Center}$ [cm ⁻²]	67 P/C-G [%H ₂ O]
CO	$2.45 \pm 1.92 \times 10^{18}$	$5.57 \pm 0.52 \times 10^{17}$	7.9×10^{16}	2.6×10^{17}	1.1×10^{20}	3.1 ± 0.9
CS	$1.4 \pm 1.03 \times 10^{14}$	2.9×10^{13}	—	—	3.9×10^{15}	0.006 ± 0.01 (CS ₂)
SO	$2.7 \pm 1.1 \times 10^{14}$	$6.6 \pm 9.0 \times 10^{13}$	3.4×10^{16}	1.3×10^{16}	4.4×10^{14}	0.071 ± 0.14
SO ₂	$1.1 \pm 0.1 \times 10^{14}$	$2.2 \pm 1.2 \times 10^{13}$	—	—	1.3×10^{15}	0.127 ± 0.25
HCO ⁺	$1.21 \pm 0.89 \times 10^{15}$	$6.8 \pm 6.6 \times 10^{13}$	—	—	—	—
H ₂ CO	$1.4 \pm 1.03 \times 10^{14}$	$3.0 \pm 0.6 \times 10^{13}$	5.6×10^{15}	1.9×10^{15}	1.9×10^{18}	0.32 ± 0.1
CH ₃ OH	$1.4 \pm 0.3 \times 10^{15}$	$3.9 \pm 1.0 \times 10^{13}$	2.5×10^{18}	7.2×10^{17}	1.0×10^{19}	0.21 ± 0.06
HCN	$2.57 \pm 1.89 \times 10^{15}$	$1.5 \pm 1.7 \times 10^{14}$	—	—	5.0×10^{16}	0.14 ± 0.04
CN	$9.90 \pm 7.37 \times 10^{15}$	$1.2 \pm 0.4 \times 10^{15}$	—	—	—	—

Table 6: Column densities for L1551 outflow (cm⁻²) are reported in our central outflow and the average of the 3 branch locations in comparison to IRAS 20126+4104 from [Palau et al. \(2017\)](#) and the abundances in 67P/C-G relative to water. Additionally we include the column densities from IRAS 16293-2422 B in the study by [Drozdovskaya et al. \(2018\)](#). Standard deviation reported for L1551 Outflow.

H₂CO can form in both in ice and in gas. This may suggest that we are seeing mainly ice sublimation chemistry in the L1551 outflow, or that we are tracing ice mantles with peculiar compositions.

5.2. Species Comparison with Comets

Now we move from comparing L1551 to other protostellar systems to comparing with comets. Specifically, we look at 67P/C-G to discuss comparisons to the comparisons made by [Drozdovskaya et al. \(2018\)](#) with IRAS 16293-2422 B. In order of abundance, the most prominent species on 67P/C-G are H_2O , O_2 , CO , CH_3OH , and H_2CO . We note that we cannot observe lines for H_2O and O_2 in L1551 because they are present in earth's atmosphere. We find that six of our nine most prominent species are reported in their report of 67P/G-C. Using our computed column densities we make comparisons to cometary abundances for our most prominent species, similarly to [Drozdovskaya et al. \(2018\)](#).

Figure 15 shows the comparison of the species between L1551 in the central protostar and comet abundances on 67P/C-G. We find significant differences in the relative abundances of different species. For example, in L1551 we find more SO than SO_2 , while in contrast, in the comet there is more SO_2 than SO . Similarly, in L1551 we find more HCN than CH_3OH and more CH_3OH than H_2CO . We see the reverse of this in the comet. Both the comet and L1551 are consistent in their relative high abundance of CO compared to other species. However, we do not seek to directly compare our CO abundances as we have established a lower limit on CO density given its optical thickness. Note in Figure 16, we compare CS in L1551 to CS_2 in 67P/C-G. This assumes an upper limit where all CS radicals are converted into CS_2 , as was similarly assumed by [Drozdovskaya et al. \(2018\)](#). CS , HCO^+ , and CN were absent in the study of the comet. To expand on these comparisons, we explore the ratios of these species to one another at different locations of L1551 in comparison with the ratios found in comet 67P/C-G.

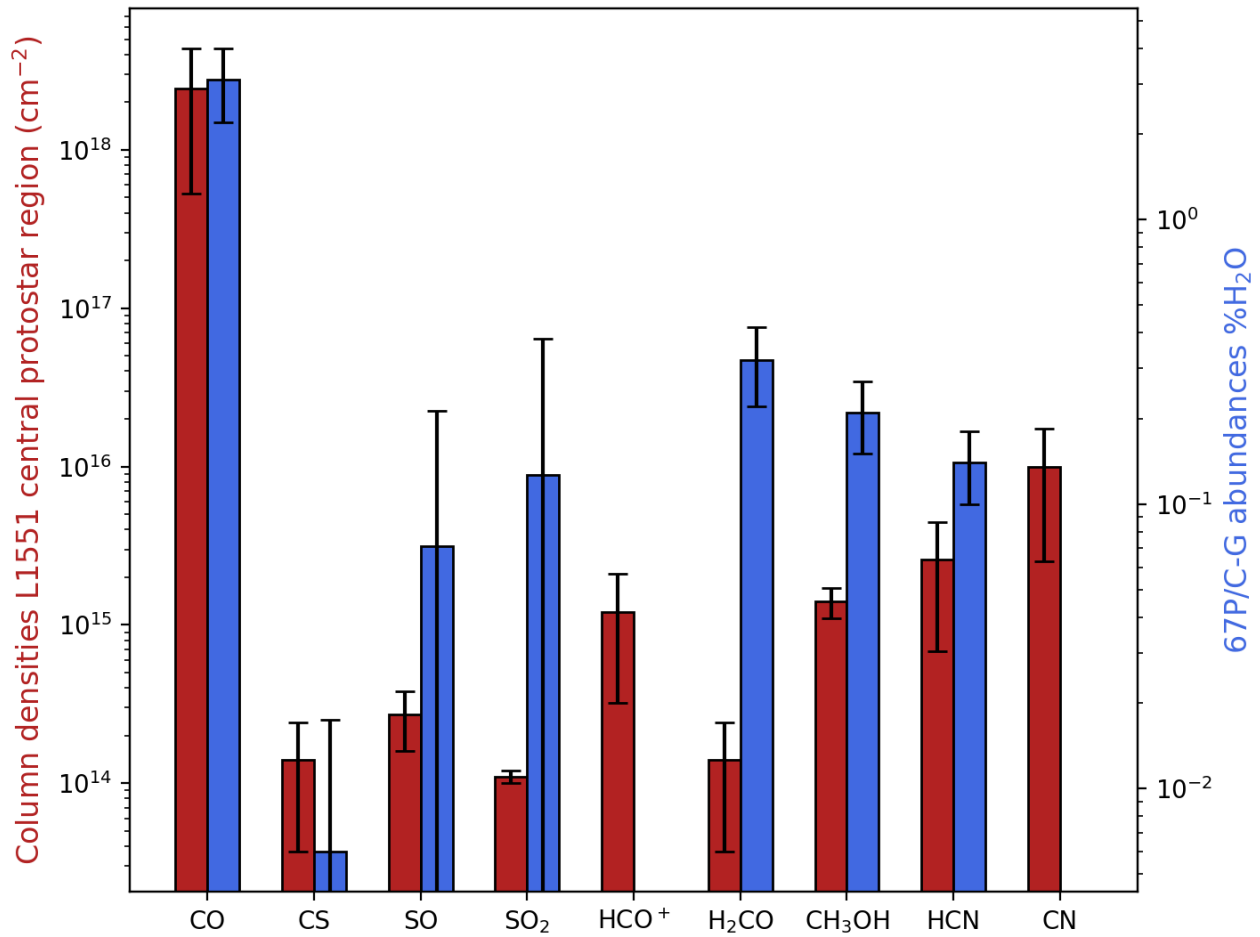


Figure 15: Comparison of abundances in central region of L1551 IRS5 to comet abundances in 67P/C-G. Note that for 67P/C-G we compare CS₂ to the CS in L1551. Red bars corresponding to the left axis represent column density in L1551, and blue bars represent abundance relative to water as a percentage on the right axis. This chart demonstrates that there are differences in the relative amounts of different species (e.g., there is more SO than SO₂ in L1551, and more SO₂ than SO in the comet).

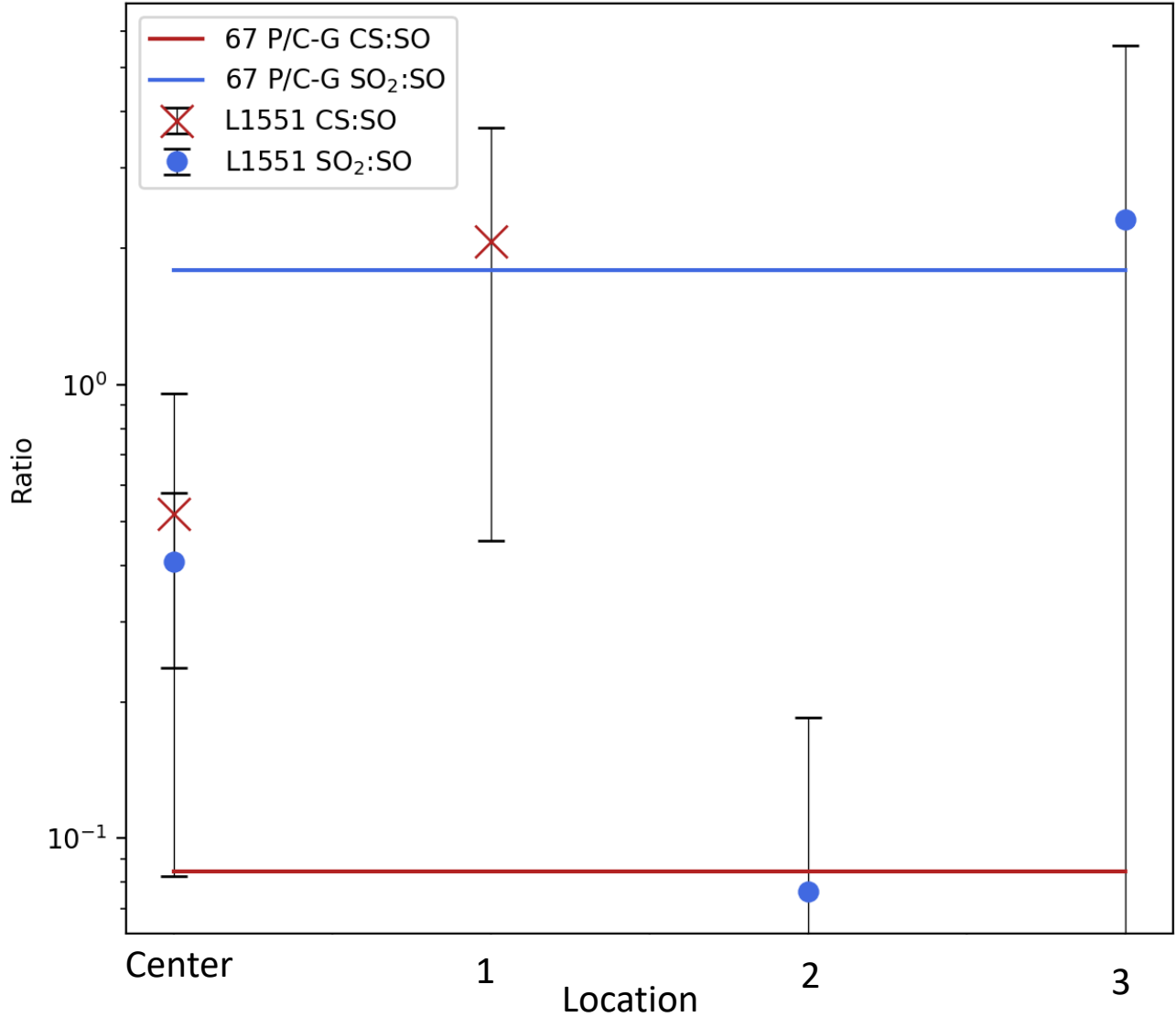


Figure 16: Ratios of CS:SO and SO₂:SO in the center of L1551 and the three locations along the outflow. Scatter points correspond to the ratio in column density in L1551 at the locations. Solid lines mark the ratio seen in 67P/C-G as a point of reference. Red color indicates CS:SO ratios, and blue features mark the SO₂:SO ratios.

Figure 16 looks at the ratios of sulfur-bearing species across the regions of the center and northeast branch of L1551 in comparison with the comet. Both the ratios for CS:SO and SO₂:SO are between

0 and 3 in all L1551 locations and the comet. We find that 67P/C-G has a lower ratio of CS:CO in the center and location 1 of the outflow. As we did not calculate column densities for CS in locations 2 and 3, it is difficult to make a direct comparison. The SO₂:SO ratio shows some variation across the outflow, less than an order of magnitude. We find the CS:SO ratio is higher in the outflow than in the comet, and the SO₂:SO ratio is lower than in the comet (with the exception of location 3). The higher CS:SO ratio implies that there is more sulfur in the oxidized form in the comet than in the protostar. Overall, there is no obvious mismatch between the comet and the protostar if you were to integrate over all protostellar regions. However, the large variation across the protostellar structure makes it very important to compare comets with all protostellar environments, not just a single point.

Figure 17 explores the ratios in organics. The ratio of HCN to H₂CO shows order of magnitude variation across the outflow. For HCN:H₂CO and CH₃OH: H₂CO the ratio falls between 0 and 9 for all locations and the comet and are thus all similar by an order of magnitude. For the CH₃OH/H₂CO ratio, they fall within a factor of two in all locations. The ratio of CH₃OH: H₂CO decreases across the outflow, between the center and location 2, and then ticks back up at location 3. Location 3 seems to be the most similar with the comet in terms of the HCN/H₂CO ratio; it is within a factor of 2 of the comet. The closest ratio of these species to that of the comet falls between location one and two or between location 1 and 3 with both ratios being within less than a factor of two of the comet.

Figure 18 depicts the change in column density for our nine species of interest as a function of radial distance out from the center center protostar. We see a decrease in nearly all species of more than an order of magnitude in column density between the center and location 1 of the outflow. We

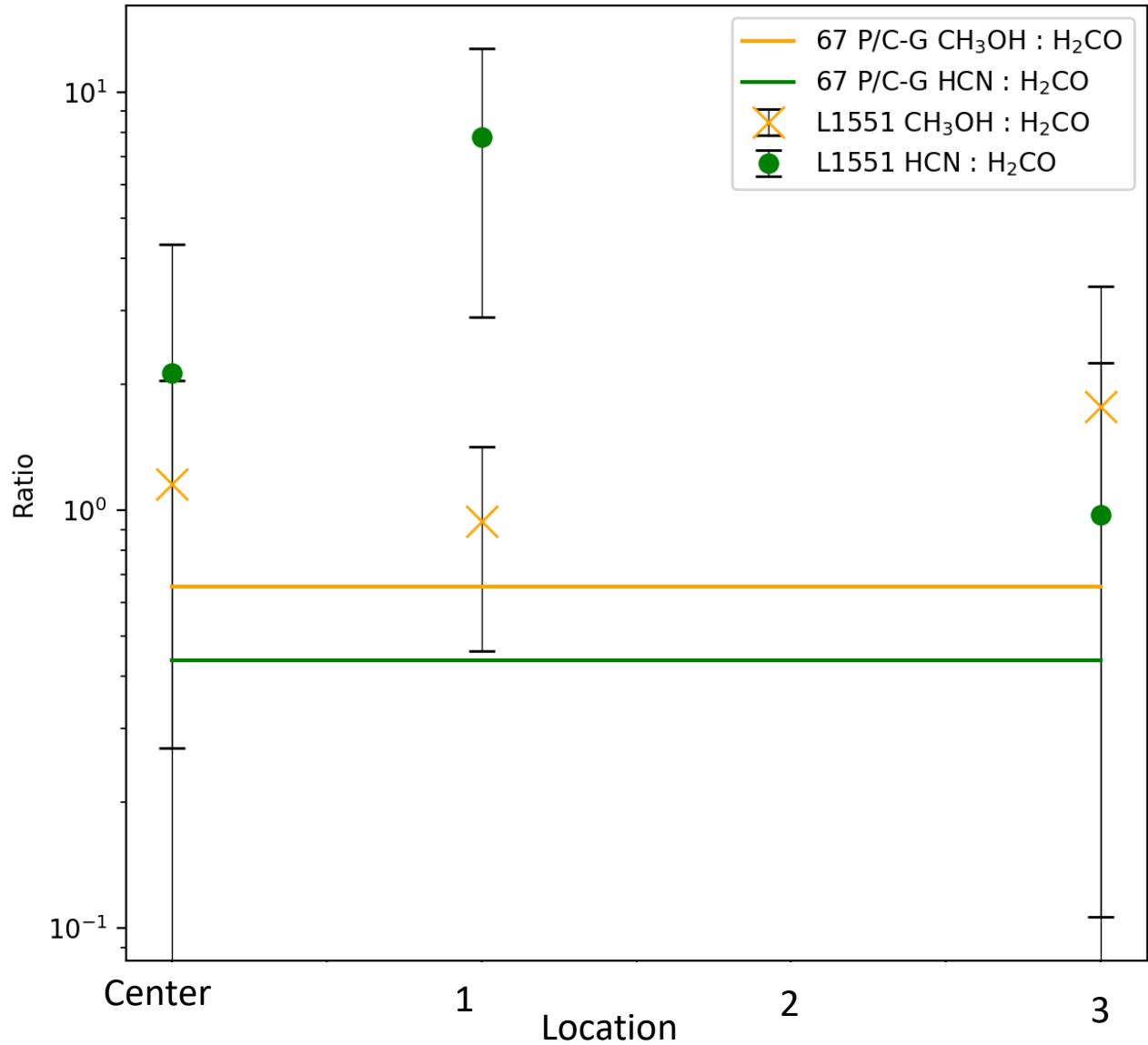


Figure 17: Ratios of $\text{CH}_3\text{OH}:\text{H}_2\text{CO}$ and $\text{HCN}:\text{H}_2\text{CO}$ in the center of L1551 and the three locations along the outflow. Scatter points correspond to the ratio in column density in L1551 at the locations. Solid lines mark the ratio seen in 67P/C-G as a point of reference. Orange color indicates $\text{CH}_3\text{OH}:\text{H}_2\text{CO}$ ratios, and green features mark the $\text{HCN}:\text{H}_2\text{CO}$ ratios.

also see the uptick in column density towards the edge of the outflow in location 3. This rise in location 3 is particularly notable for CO, SO_2 , and CH_3OH where the density at location 3 is greater

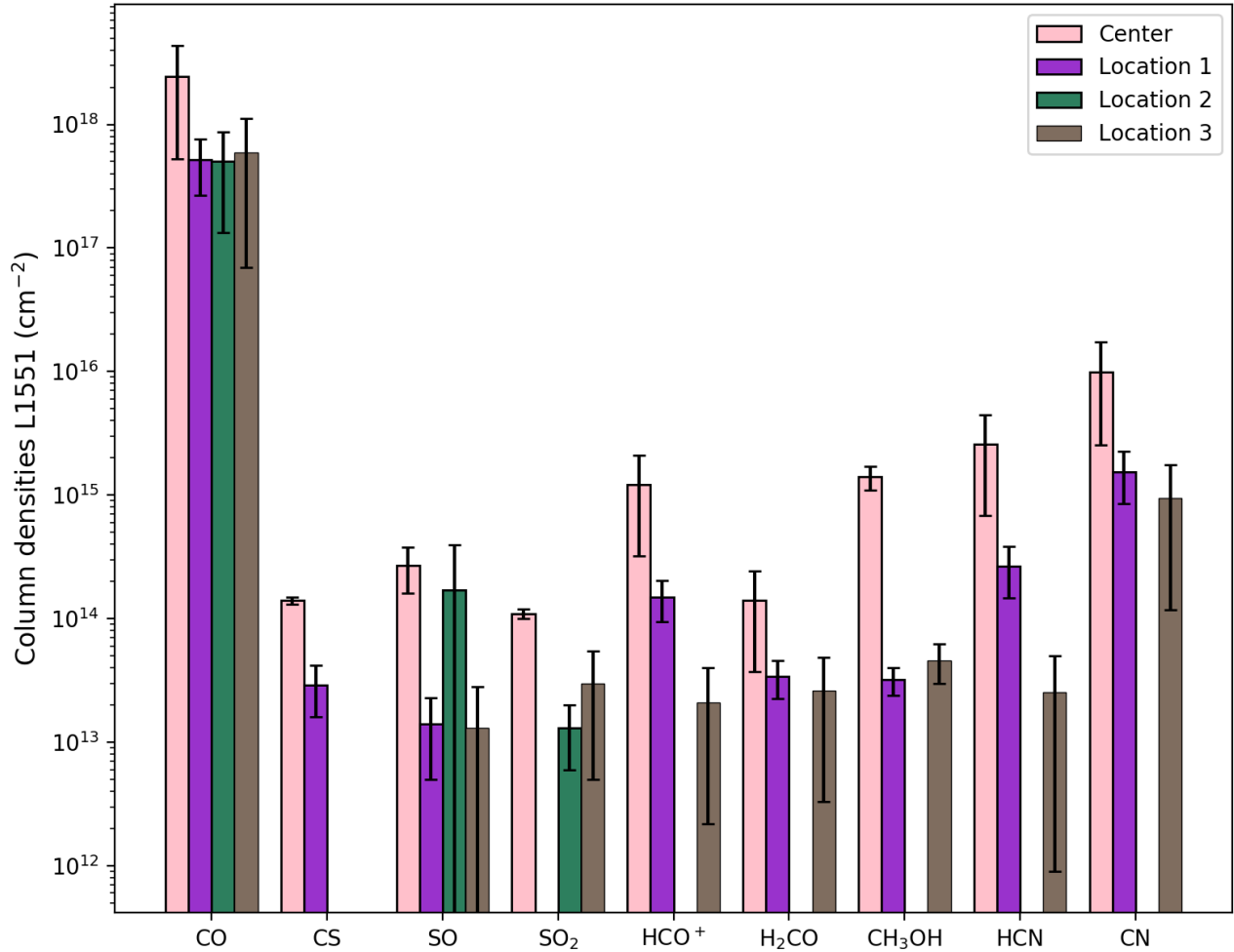


Figure 18: Column Densities of L1551 IRS5 as grouped by species. Bars correspond to the center region and locations 1 through 3 in the northeast branch. The log scale shows the steep decrease in column density from the central protostar to the outflows. We do not have measured densities for several species in location 2. Several species show an increase again in location 3 closer to the edges of the outflow.

than that at location 1. Location 2 is notably absent for several species. CO and the similar sulfur bearing species, SO and SO₂, are still present in location 2. This perhaps indicates of a higher O/C ratio in location 2 than other areas of the outflow.

Overall, we find there is variation of the ratios of sulfur bearing and organic species as a function of distance from the central protostar. We find better agreement between comet and protostellar abundance ratios when comparing 67P/C-G with outer outflow regions, than with the inner outflow regions or the central protostar. This trend may suggest that we are indeed seeing the ice chemistry with the shocks. Specifically, by finding better agreement farther away from the protostar suggests that we are probing pristine ice desorption as there is too much heating close in. Based on the overall similarities in the outflow, we believe that we are likely identifying the surrounding icy cloud as sublimated into the gas phase through shocks in the outflow.

6. CONCLUSIONS

To understand the chemistry which makes life possible in our solar system, we must look at earlier stages of star formation. However, it can be difficult to probe chemistry through ice observations. Thus, we look to protostellar outflows with sputtering molecules from the transitioning ice into gas without inducing thermal processes as a proxy for observing ice chemistry directly. Here, we analyze observations taken from the Atacama Compact Array of the object L1551 IRS5, a multiple protostar system with distinct outflows. With these observations we:

- (1) calculate the rotational temperatures and column densities of nine species (CO, CS, SO, SO₂, HCO⁺, H₂CO, CH₃OH, HCN, and CN), across the outflow, and find order of magnitude changes in column densities across the outflow.
- (2) find column density ratios change significantly across the outflow, implying a changing chemistry away from the central protostar with distinct chemical processes along the outflow.
- (3) compare L1551 to another protostar, IRAS 16293, and note a more drastic falloff in column density, especially in larger species, suggesting there are weaker shocks in the outflow and less sputtering than in the outflow of IRAS 16293.
- (4) see six of our nine most prominent species present in 67P/G-C both consistent in CO being the most abundant of these 9, and consistently higher densities of organics than sulfur-bearing species.
- (5) find the ratios of different species in L1551 are more similar to the comet in the outflows, especially further out, suggesting that we are perhaps seeing more material sputtered into the ice there.

Overall, we find complex chemistry in both the central protostar and the outflow of L1551 IRS5. We note how chemical densities vary at different distances along the outflow. Based on the enumerated findings above, we conclude that this outflow may be a proxy for the ice chemistry in the system. By understanding this system and ultimately applying this method to other systems in the future, we hope to better understand the overall chemistry of stellar evolution.

REFERENCES

- Altwegg, K., Balsiger, H., Bar-Nun, A., et al. 2016, *Science Advances*, 2, e1600285
- Altwegg, K., Balsiger, H., & Fuselier, S. A. 2019, *ARA&A*, 57, 113
- Arce, H. G., Shepherd, D., Gueth, F., et al. 2007, *Protostars and Planets V*, 245
- Biegging, J. H., & Cohen, M. 1985, *ApJL*, 289, L5
- Blake, G. A., Sutton, E. C., Masson, C. R., et al. 1987, *ApJ*, 315, 621
- Bockelée-Morvan, D., Lis, D. C., Wink, J. E., et al. 2000, *A&A*, 353, 1101
- Boogert, A. C. A., Gerakines, P. A., & Whittet, D. C. B. 2015, *ARA&A*, 53, 541
- Burkhardt, A. M., Dollhopf, N. M., Corby, J. F., et al. 2016, *ApJ*, 827, 21
- Burkhardt, A. M., Shingledecker, C. N., Le Gal, R., et al. 2019, *ApJ*, 881, 32
- Condon, J., & Ransom, S. 2016, *Essential radio astronomy (Vol. 2)* Princeton University Press
- Cruz-Sáenz de Miera, F., Kóspál, Á., Ábrahám, P., et al. 2019, *ApJL*, 882, L4
- Drozdovskaya, M. N., van Dishoeck, E. F., Jørgensen, J. K., et al. 2018, *MNRAS*, 476, 4949
- Ehrenfreund, P., & Charnley, S. B. 2000, *ARA&A*, 38, 427
- Elsila, J. E., Glavin, D. P., & Dworkin, J. P. 2009, *Meteoritics and Planetary Science*, 44, 1323
- Fridlund, C. V. M., Bergman, P., White, G. J., et al. 2002, *A&A*, 382, 573
- Fridlund, M. 2016, arXiv e-prints, arXiv:1603.06704
- Garrod, R. T. 2013, *ApJ*, 765, 60
- Hadraoui, K., Cottin, H., Ivanovski, S. L., et al. 2019, *A&A*, 630, A32
- Herbst, E., & Millar, T. 2008, *The chemistry of cold interstellar cloud cores, in low temperatures and cold molecules*, ed. I. W. M. Smith (London, England: Imperial College Press)
- Lissauer, J. J. 1993, *ARA&A*, 31, 129
- McGuire, B. A., Carroll, P. B., Loomis, R. A., et al. 2016, *Science*, 352, 1449
- Mumma, M. J., & Charnley, S. B. 2011, *ARA&A*, 49, 471
- Öberg, K. I., Boogert, A. C. A., Pontoppidan, K. M., et al. 2011, *ApJ*, 740, 109
- Palau, A., Walsh, C., Sánchez-Monge, Á., et al. 2017, *MNRAS*, 467, 2723
- Requena-Torres, M. A., Martín-Pintado, J., Rodríguez-Franco, A., et al. 2006, *A&A*, 455, 971
- Ruud, M., Wakelam, V., & Hersant, F. 2016, *MNRAS*, 459, 3756
- Rubin, M., Altwegg, K., Balsiger, H., et al. 2019, *MNRAS*, 489, 594
- Sandqvist, A., & Bernes, C. 1980, *A&A*, 89, 187
- Shu, F. H., Lizano, S., & Adams, F. C. 1987, *Star Forming Regions*, 417
- Snyder, L. E., Lovas, F. J., Hollis, J. M., et al. 2005, *ApJ*, 619, 914
- Suutarinen, A. N., Kristensen, L. E., Mottram, J. C., et al. 2014, *MNRAS*, 440, 1844
- Visser, R., van Dishoeck, E. F., Doty, S. D., et al. 2009, *A&A*, 495, 881
- Walsh, C., Millar, T. J., Nomura, H., et al. 2014, *A&A*, 563, A33
- Wu, P.-F., Takakuwa, S., & Lim, J. 2009, *ApJ*, 698, 184

7. ACKNOWLEDGEMENTS

This thesis could not have been possible without all of the amazing help and support I have gotten. I want to start by thanking the teachers of the Astro and EPS 99 thesis courses, Dr. Esther James, Dr. John Kovac, Dr. Ramesh Narayan, and Dr. Annika Quick for their help over the year. I want to thank my academic advisors Dr. David Charbonneau and Dr. Roger Fu for their guidance throughout my time at Harvard. I want to thank Dr. David Wilmer and Dr. Robin Wordsworth for committing time to reading my thesis and providing insightful feedback. Thank you to all my professors at Harvard for inspiring me everyday to always give it my all, learn a lot, and have fun doing it. I also want to thank my high school teachers who inspired me to love science. I'd like to give a huge thank you to my friends and family (including Apollo) for all their fun and support, and especially my parents for all their love and care. And most of all, I want to thank my incredible thesis advisors Dr. Andrew Burkhardt and Dr. Karin Öberg. Dr. Andrew Burkhardt, thank you for all your patience, endless help, reassurance, and for always knowing exactly how to answer my many many questions. Dr. Karin Öberg, thank you for teaching me everything I know about astrochemistry, for putting so much care and detail into helping me learn and grow, and for your enthusiasm which has made this project so special to me. Academically, and beyond this project, you have both been incredible role models, and I am grateful to have had the opportunity to work with you over the past two years!

8. APPENDIX

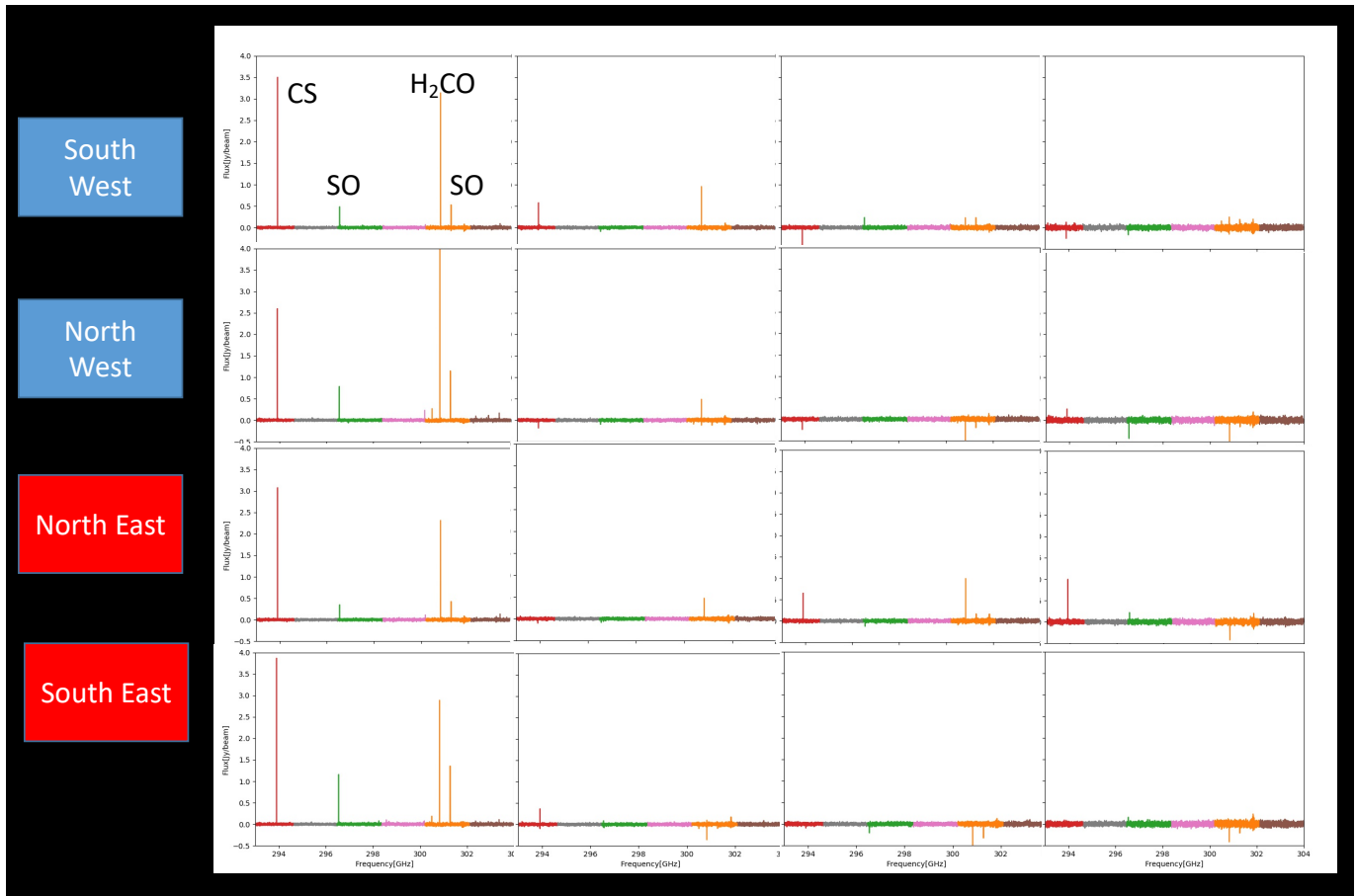


Figure 19: This figure shows spectra across the 16 outflow regions from 293 to 304 GHz showing transitions for CS, SO, and H₂CO. From left to right, the panels show location 1, 2, 3, and 4.

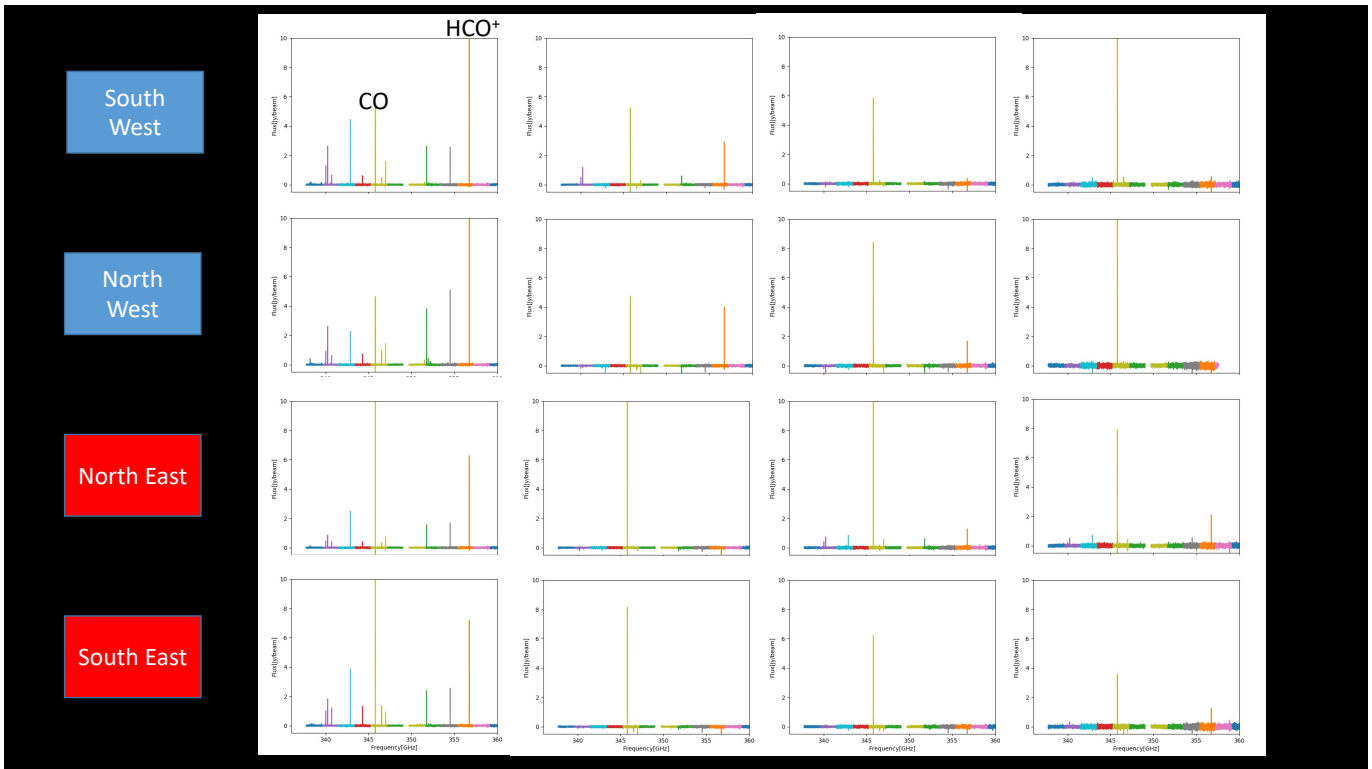


Figure 20: This figure shows spectra across the 16 outflow regions from 340 to 360 GHz. This figure hosts the transitions with high flux from CO and HCO⁺. From left to right, the panels show location 1, 2, 3, and 4.

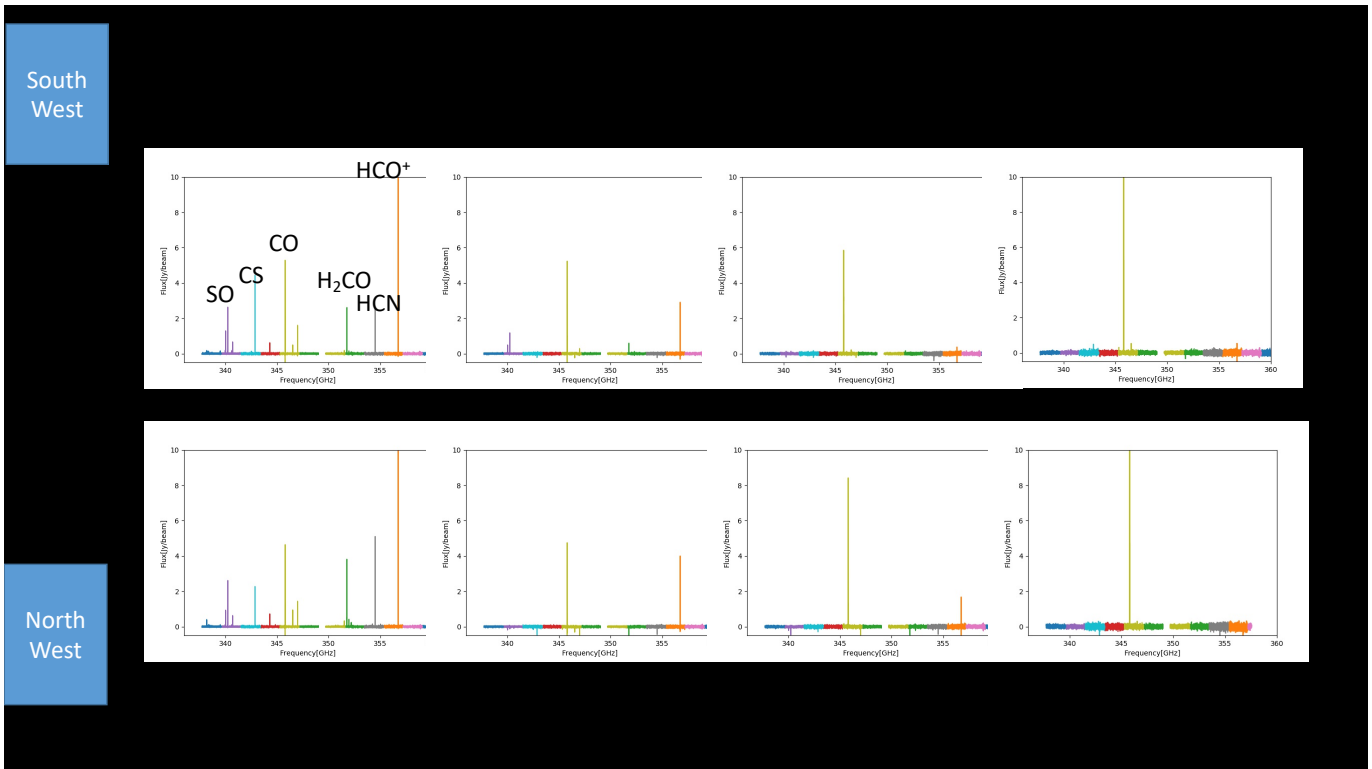


Figure 21: This figure is a zoom-in of Figure 20, examining more transitions and focusing on the western branches across the 8 outflow regions. From left to right, the panels show location 1, 2, 3, and 4.

Species	Branch	Number	Xo km/s	Io Jy/beam	FWHM km/s	Integrated Intensity Jy/beam km/s
CS	Center	Center	2.36±0.03	8.85±0.21	2.36±0.06	20.86±0.75
CS	SW	1	6.44±0.02	3.81±0.11	1.63±0.06	6.23±0.28
CS	SW	2	6.36±0.03	0.61±0.04	1.32±0.06	0.81±0.06
CS	SW	3	—	—	—	—
CS	SW	4	8.96±0.21	0.12 ±0.04	1.69±0.47	0.21±0.09
CS	NW	1	6.89±0.01	2.77±0.05	1.64±0.03	4.55±0.11
CS	NW	2	—	—	—	—
CS	NW	3	—	—	—	—
CS	NW	4	6.45±0.17	0.29±0.04	3.25±0.39	0.94±0.18
CS	NE	1	6.84±0.02	3.35±0.09	1.84±0.05	6.18±0.24
CS	NE	2	12.63±1.82	0.01±0.10	1.36±12.33	0.02±0.21
CS	NE	3	6.51±0.04	0.76±0.07	1.48±0.16	1.12±0.16
CS	NE	4	6.80±0.07	1.01±0.07	2.13±0.16	2.15±0.23
CS	SE	1	6.29±0.02	3.89±0.09	1.87±0.04	7.27±0.23
CS	SE	2	6.08±	0.4356±	0.24±	0.11±.05
CS	SE	3	—	—	—	—
CS	SE	4	5.96±0.32	0.09±0.04	2.75±0.76	0.24±0.12

Species	Branch	Number	Xo km/s	Io Jy/beam	FWHM km/s	Integrated Intensity Jy/beam km/s
HCO ⁺	Center	Center	6.56±0.10	21.39±1.34	3.29±0.24	70.39±6.72
HCO ⁺	SW	1	5.95± 0.02	12.60±0.33	1.64±0.05	20.61±0.81
HCO ⁺	SW	2	6.13±0.59	4.28±13.99	0.67±1.24	2.86±10.76
HCO ⁺	SW	3	—	—	—	—
HCO ⁺	SW	4	—	—	—	—
HCO ⁺	NW	1	6.38±0.05	13.89±0.75	1.78±0.11	24.73±2.04
HCO ⁺	NW	2	6.24±0.04	4.96±0.50	1.20±0.16	5.98±0.98
HCO ⁺	NW	3	6.12±1.99	2.27±19.73	0.71±4.12	1.62±16.90
HCO ⁺	NW	4	—	—	—	—
HCO ⁺	NE	1	7.39±0.09	6.36±0.74	1.26±0.17	7.99±1.41
HCO ⁺	NE	2	—	—	—	—
HCO ⁺	NE	3	6.77±0.12	1.27±0.19	1.27±0.20	1.61±0.35
HCO ⁺	NE	4	7.01±0.04	2.28±0.13	1.66±0.10	3.78±0.32
HCO ⁺	SE	1	5.30±0.12	7.65±1.33	1.42±0.29	10.84±2.92
HCO ⁺	SE	2	—	—	—	—
HCO ⁺	SE	3	—	—	—	—
HCO ⁺	SE	4	5.55±0.52	2.03±10.02	0.79±2.69	1.61±9.62

Species	Branch	Number	Xo km/s	Io Jy/beam	FWHM km/s	Integrated Intensity Jy/beam km/s
SO	Center	0	6.67±0.05	3.84±0.15	2.85±0.12	10.96±0.64
SO	SW	1	6.15±0.08	0.50±0.06	1.28±0.15	0.64±0.11
SO	SW	2	—	—	—	—
SO	SW	3	6.37±0.28	0.21±0.08	1.28±0.51	0.27±0.15
SO	SW	4	6.83±0.10	0.50±0.04	4.60±0.24	2.30±0.22
SO	NW	1	6.91±0.04	1.01±0.07	1.30±0.09	1.32±0.13
SO	NW	2	—	—	—	—
SO	NW	3	—	—	—	—
SO	NW	4	6.20±0.47	0.26±0.05	6.90±1.31	1.83±0.48
SO	NE	1	6.58±0.21	0.40±0.39	0.98±0.93	0.39±0.53
SO	NE	2	5.17±0.33	0.12±0.12	2.23±0.85	0.27±0.30
SO	NE	3	6.55±1.79	0.21±1.87	0.83±5.68	0.17±1.95
SO	NE	4	—	—	—	—
SO	SE	1	6.05±0.03	1.40±0.05	1.64±0.06	2.30±0.12
SO	SE	2	—	—	—	—
SO	SE	3	—	—	—	—
SO	SE	4	—	—	—	—

Species	Branch	Number	Xo km/s	Io Jy/beam	FWHM km/s	Integrated Intensity Jy/beam km/s
H ₂ CO	Center	Center	6.55±0.02	7.68±0.11	2.97±0.05	22.78±0.47
H ₂ CO	SW	1	6.06±0.01	3.12±0.05	1.57±0.02	4.92±0.11
H ₂ CO	SW	2	6.09±0.02	0.95±0.03	1.13±0.02	1.07±0.04
H ₂ CO	SW	3	6.09±0.39	0.22±0.06	3.81±0.95	0.82±0.29
H ₂ CO	SW	4	5.04±0.33	0.24±0.09	1.56±0.60	0.38±0.21
H ₂ CO	NW	1	6.61±0.02	5.36±0.11	2.02±0.05	10.86±0.34
H ₂ CO	NW	2	6.58±0.08	0.86±2.87	1.04±2.85	0.90±3.87
H ₂ CO	NW	3	—	—	—	—
H ₂ CO	NW	4	—	—	—	—
H ₂ CO	NE	1	6.67±0.02	2.66±0.06	1.83±0.05	4.86±0.17
H ₂ CO	NE	2	6.16±0.16	0.47±0.05	0.92±0.17	0.44±0.09
H ₂ CO	NE	3	6.35±0.05	1.04±0.07	1.67±0.11	1.74±0.16
H ₂ CO	NE	4	—	—	—	—
H ₂ CO	SE	1	6.09±0.02	2.87±0.07	2.38±0.06	6.82±0.22
H ₂ CO	SE	2	—	—	—	—
H ₂ CO	SE	3	—	—	—	—
H ₂ CO	SE	4	—	—	—	—

Species	Branch	Number	Xo km/s	Io Jy/beam	FWHM km/s	Integrated Intensity Jy/beam km/s
CO	Center	Center	6.19±1.12	8.30±1.42	13.43±2.75	111.48±29.72
CO	NE	1	8.45±	16.54±0.03	2.05±	33.84±0.06
CO	NE	2	8.86±0.17	11.65±1.44	2.89±0.41	33.68±6.35
CO	NE	3	8.91±0.20	11.77±1.51	3.22±0.48	37.85±7.48
HCN	center	0	6.64±0.03	9.32±0.21	3.15±0.08	29.32±0.99
HCN	NE	1	6.84±0.02	1.92±0.05	1.88±0.05	3.60±0.14
HCN	NE	2	—	—	—	—
HCN	NE	3	7.53±0.24	0.19±0.06	1.98±0.57	0.38±0.16

Species	Branch	Number	Xo km/s	Io Jy/beam	FWHM km/s	Integrated Intensity Jy/beam km/s
CN	center	0	6.44 ± 0.12	2.95 ± 0.23	3.17 ± 0.28	9.34 ± 1.10
CN	NE	1	6.83 ± 0.07	0.88 ± 0.06	2.44 ± 0.15	2.15 ± 0.20
CN	NE	2	—	—	—	—
CN	NE	3	6.24 ± 0.03	0.86 ± 0.06	1.45 ± 0.10	1.25 ± 0.12
CH ₃ OH	Center	Center	8.56 ± 0.10	1.01 ± 0.06	3.81 ± 0.23	3.86 ± 0.33
CH ₃ OH	NE	1	8.70 ± 0.24	0.05 ± 0.03	2.37 ± 0.57	0.11 ± 0.08
CH ₃ OH	NE	2	—	—	—	—
CH ₃ OH	NE	3	7.05 ± 0.73	0.02 ± 0.04	1.34 ± 1.30	0.03 ± 0.06

Table 7: This table presents a summary of fitting spectral peaks and the corresponded integrated intensity calculated for different species in the four regions at the strongest transition (Table 2). Some species were only calculated for the northeast branch. “Xo” denotes the offset from the central velocity of a transition in the database. Note that many concur with the around VLSR 6.5 km/s. Error on Xo based on the gaussian fit. “Io” denotes the peak flux of the spectral feature. Error on Io calculated to include both the error on the gaussian fit and the noise of our observations. “FWHM” is the full width half max of the gaussian with corresponding error for the fit. Using the gaussian fit, we calculate the integrated intensity as the area under the curve with error from propagation of gaussian fit. Dashed lines indicate no detectable fit to a spectral feature at the predominant transition.